

AD-A031 740

AIR FORCE MATERIALS LAB WRIGHT-PATTERSON AFB OHIO  
GALLIUM DIFFUSION IN SILICON DIOXIDE. RUTHERFORD BACKSCATTERING--ETC(U)  
MAY 76 P M HEMENGER  
AFML-TR-75-55

F/G 7/2

UNCLASSIFIED

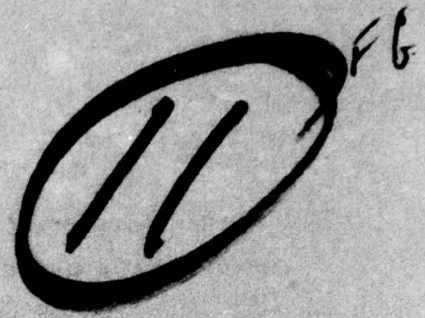
NL

1 OF 2  
AD  
A031740



ADA031740

AFML-TR-75-55



## GALLIUM DIFFUSION IN SILICON DIOXIDE

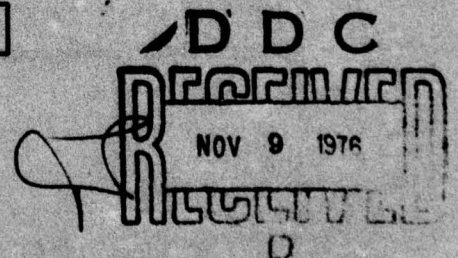
*RUTHERFORD BACKSCATTERING ANALYSIS OF THIN FILMS*

*LASER AND OPTICAL MATERIALS BRANCH  
ELECTROMAGNETIC MATERIALS DIVISION*

MAY 1976

TECHNICAL REPORT AFML-TR-75-55  
FINAL REPORT FOR PERIOD 1 SEPTEMBER 1973 - 28 AUGUST 1974

Approved for public release; distribution unlimited



AIR FORCE MATERIALS LABORATORY  
AIR FORCE WRIGHT AERONAUTICAL LABORATORIES  
AIR FORCE SYSTEMS COMMAND  
WRIGHT-PATTERSON AIR FORCE BASE, OHIO 45433




NOTICE

82-27-91-1M3A

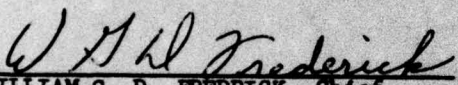
When Government drawings, specifications, or other data are used for any purpose other than in connection with a definitely related Government procurement operation, the United States Government thereby incurs no responsibility nor any obligation whatsoever; and the fact that the government may have formulated, furnished, or in any way supplied the said drawings, specifications, or other data, is not to be regarded by implication or otherwise as in any manner licensing the holder or any other person or corporation, or conveying any rights or permission to manufacture, use, or sell any patented invention that may in any way be related thereto.

This report has been reviewed by the Information Office (IO) and is releasable to the National Technical Information Service (NTIS). At NTIS, it will be available to the general public, including foreign nations.

This technical report has been reviewed and is approved for publication.

  
PATRICK M. HEMENGER  
Project Monitor

FOR THE COMMANDER

  
WILLIAM G. D. FREDRICK, Chief  
Laser & Optical Materials Branch  
Electromagnetic Materials Division

Copies of this report should not be returned unless return is required by security considerations, contractual obligations, or notice on a specific document.

AIR FORCE MATERIALS LABORATORY  
AIR FORCE WRIGHT AERONAUTICAL LABORATORIES  
AIR FORCE SYSTEMS COMMAND  
WRIGHT-PATTERSON AIR FORCE BASE, OHIO 45433

UNCLASSIFIED

SECURITY CLASSIFICATION OF THIS PAGE (When Data Entered)

REPORT DOCUMENTATION PAGE		READ INSTRUCTIONS BEFORE COMPLETING FORM
1. REPORT NUMBER AFML-TR-75-55	2. GOVT ACCESSION NO.	3. RECIPIENT'S CATALOG NUMBER Final Rept.
4. TITLE (and subtitle) GALLIUM DIFFUSION IN SILICON DIOXIDE Rutherford Backscattering Analysis of Thin Films.		5. TYPE OF REPORT & PERIOD COVERED 1 Sep 1973 - 28 Aug 1974
7. AUTHOR(s) Patrick M. Hemenger		6. PERFORMING ORG. REPORT NUMBER
9. PERFORMING ORGANIZATION NAME AND ADDRESS Air Force Materials Laboratory (AFML/LPO) Air Force Systems Command Wright-Patterson Air Force Base, Ohio 45433		8. CONTRACT OR GRANT NUMBER(s)
11. CONTROLLING OFFICE NAME AND ADDRESS Air Force Materials Laboratory (AFML/LPO) Air Force Systems Command Wright-Patterson Air Force Base, Ohio 45433		10. PROGRAM ELEMENT, PROJECT, TASK AREA & WORK UNIT NUMBERS
14. MONITORING AGENCY NAME & ADDRESS (if different from Controlling Office)		12. REPORT DATE May 1976
		13. NUMBER OF PAGES 101
		15. SECURITY CLASS. (of this report) Unclassified
		15a. DECLASSIFICATION/DOWNGRADING SCHEDULE
16. DISTRIBUTION STATEMENT (of this Report)  Approved for public release; distribution unlimited.		
17. DISTRIBUTION STATEMENT (of the abstract entered in Block 20, if different from Report)		
18. SUPPLEMENTARY NOTES		
19. KEY WORDS (Continue on reverse side if necessary and identify by block number) Rutherford Backscattering Gallium Diffusion Silicon Dioxide Thin Films		
20. ABSTRACT (Continue on reverse side if necessary and identify by block number) The behavior of Ga in sputtered SiO <sub>2</sub> films is examined with the result that diffusion is observed during annealing at 850°C. The accumulated evidence indicates that SiO <sub>2</sub> is not an effective film to use on a GaP or GaAs for protection against Ga loss during high temperature anneals.  The method employed to make the measurements, Rutherford backscattering (RBS) analysis of SiO <sub>2</sub> :Ga:SiO <sub>2</sub> sandwiches, is demonstrated to be effective and applicable to other systems.		

DD FORM 1 JAN 73 1473 EDITION OF 1 NOV 65 IS OBSOLETE

UNCLASSIFIED

SECURITY CLASSIFICATION OF THIS PAGE (When Data Entered)

012320

JB



UNCLASSIFIED

SECURITY CLASSIFICATION OF THIS PAGE(When Data Entered)

The value of RBS as a general tool for thin film analysis is demonstrated by measuring the thicknesses and compositions of several types of films as well as the concentrations and locations of impurities. ←

ACCESSION No.	
NTIS	White Section <input checked="" type="checkbox"/>
DDC	Buff Section <input type="checkbox"/>
UNANNOUNCED	<input type="checkbox"/>
JUSTIFICATION	
BY	
DISTRIBUTION/AVAILABILITY CODES	
Dist.	AVAIL and/or SPECIAL
A	

DDC  
RECEIVED  
NOV 9 1976  
D

UNCLASSIFIED

SECURITY CLASSIFICATION OF THIS PAGE(When Data Entered)



## FOREWORD

The work described in this report was performed at the University of Salford, Department of Electrical Engineering, Salford, England where the author performed postdoctoral research under the Long-Term Full Time Training (LTFTT) program. This opportunity given to the author (Dr. Hemenger) by the Air Force Materials Laboratory, Air Force Systems Command, U.S. Air Force permitted him to work for a year (1 September - 28 August 1974) in a laboratory at the forefront of ion implantation research. The author gratefully acknowledges this experience and is indebted to the University of Salford for offering him the chance to join the university and to participate in their research program. As a direct result of the superb scientific environment and excellent facilities, it was possible to address and resolve a specific technical problem which was unsolvable with the background and facilities available before the LTFTT assignment. Additionally, the new techniques and skills that were acquired are now being employed for the solution of new problems.

A particular debt is owed to Professor George Carter, who, in addition to arranging the program with Salford, constantly supplied enthusiasm and ideas and furnished help both at the University and outside where he made the transition to English life smooth for the author and his family. Also essential to a successful year were the many people who worked with and discussed problems with the author, who answered questions, and who were relied upon in general. In particular, Dr. J. S. Williams assisted with the Van de Graaff accelerator and he along

AFML-TR-75-55

with Dr. W. A. Grant gave time generously in discussions and were the sources of many ideas. Professor Carter, Dr. Grant, and Dr. Williams also contributed directly to this report by reviewing in detail the first draft and suggesting a number of improvements that have been incorporated. Dr. G. A. Stephens' help with Van de Graaff problems is appreciated.

A great deal of support was given by many people including M. Nobes who performed the ion implantations and A. M. Phahle who prepared the sputtered films.

This report has been written in a tutorial vein because it is the result of a learning experience for the author and because it is being submitted to the University of Salford as the thesis requirement for a Master of Science Degree.



## TABLE OF CONTENTS

SECTION	PAGE
I INTRODUCTION	1
II RUTHERFORD BACKSCATTERING	3
1. General	3
2. Experimental Considerations and Applications	9
a. Experimental Parameters	9
b. Scattering Depth	14
c. Dopant Profile	16
d. Thin Films	17
e. Angle of Incidence	19
3. Stopping Power	26
4. Laboratory Coordinate System	30
III IMPURITY DETECTION AND STOICHIOMETRY	33
1. General	33
2. Surfaces	34
3. Bulk Compounds	35
4. Films	36
a. Silicon Oxide - Literature Review	40
b. Silicon Nitride - Literature Review	41
c. Aluminum Oxide - Literature Review	42
d. Native Oxides on III-V Semiconductors - Literature Review	43
IV ANALYSIS OF COMPOUND FILMS - EXPERIMENTAL RESULTS	45
1. Sputtered Silicon Oxide - Composition	45
2. Other Films - Compositions and Impurities	51
a. Aluminum Fluoride	51
b. Cadmium Selenide	54
c. Hafnium Oxide	57
V DIFFUSION OF GALLIUM IN ENCAPSULATING FILMS	59
1. General	59
2. Ga Diffusion in $\text{SiO}_x$ , $\text{SiN}_x$ , $\text{Al}_2\text{O}_3$ and $\text{AlN}$ - Literature Review	60
3. Diffusion of Implanted Ga in Sputtered $\text{SiO}_2$ - Experimental Results	62



## TABLE OF CONTENTS (Concluded)

SECTION	PAGE
4. Ga Diffusion in SiO <sub>2</sub> - Other Experimental Approaches	74
a. Simultaneous Implantation of Pb and Ga into SiO <sub>2</sub>	74
b. Evaporation of Ga onto SiO <sub>2</sub>	77
c. SiO <sub>2</sub> Coating on Implanted GaP	78
d. SiO <sub>2</sub> Coating on GaP Examined by Channeling	81
VI SUMMARY AND SUGGESTED FUTURE WORK	83
1. Summary	83
2. Suggested Future Work	83
APPENDIX - TABLE OF k <sup>2</sup> AND CROSS-SECTION VALUES	85
REFERENCES	87

## LIST OF ILLUSTRATIONS

FIGURE		PAGE
1	Schematic RBS (Rutherford Backscatter) Spectrum from a Random Sample. $E_0$ and $E_s$ Are the Energies of the Incident and Surface Scattered Ions, Respectively	5
2	Illustration of an Incident Beam Parallel to a Low Index (Channeling) Direction in a Two-Dimensional Lattice	7
3	Schematic RBS Spectra for Channeled and Random Orientations of a Sample. $E_0$ and $E_s$ Are the Energies of the Incident and Surface Scattered Ions, Respectively	7
4	Typical Backscattering Set-Up for a Scattering Event at a Depth $t$ in the Sample. Typically, $\phi = 168^\circ$ and $\theta_1 + \theta_2 = 12^\circ$	10
5	Schematic RBS Spectrum for an Impurity Layer (Mass = $M_i$ ) Near the Surface of a Substrate Material (Mass = $M_s$ ), Where $M_i > M_s$ . $E_0$ Is the Incident Energy of the Probe Beam	18
6	Schematic RBS Spectrum of a High Mass Substrate Coated with a Low Mass Silicon Oxide Film. The Energy $k_s^2 E_0$ Represents the "Edge" Energy for Scattering from the Substrate with No Film Present and $E_s$ Represents the Observed Edge Shifted Due to Stopping Power Losses of the Probe Particles As They Travel Into and Back Out Through the Film	18
7	Schematic RBS Spectrum for an $SiO_x$ Film	37
8	Backscatter Spectrum from a Silicon Oxide Film on a Carbon Substrate. Channel 226.7 Represents Scattering from Si on the Surface of the Film and Channel 175 from Si at the Si-C Interface, Likewise for O	47
9	Experimental Arrangement Used for Collecting the RBS Data Shown in Figure 8	47
10	RBS Spectrum from an $AlF_x$ Film on a Carbon Substrate	53
11	RBS Spectrum of an $AlF_x$ Pellet. This Specimen Was Compressed from the Powder Used to Evaporate the Film Examined in Figure 10	53
12	RBS Spectrum of a CdSe Film on a Si Substrate with a Heavy Impurity Near Channel No. 370. The Angle of Incidence is $90^\circ$ ( $\theta_1 = 0$ )	56



## LIST OF ILLUSTRATIONS (Cont'd)

FIGURE		PAGE
13	RBS Spectrum of the Sample Shown in Figure 12, but with a 30° Angle of Incidence ( $\theta_1 = 60^\circ$ )	56
14	RBS Spectrum of a $HfO_x$ Film on a Carbon Substrate ( $\theta_1 = 60^\circ$ )	58
15	Schematic Illustration of the Sandwich Structure Employed for Studying the Diffusion of Ga in $SiO_2$	63
16	RBS Spectrum of $SiO_2$ on Si. The Film Thickness is About 2610Å, Calculated Using the Shift in the Substrate Si Edge from the Surface Position (Channel No. 226.7) to Channel No. 144.5	63
17	RBS Spectrum of the Sample in Figure 16 after Implantation of Ga to a Dose of $4.0 \times 10^{16}/cm^2$ . The Ga Edge is Calculated to Appear at Channel No. 318.6	65
18	RBS Spectrum of the Sample in Figure 17 After the Addition of a $SiO_2$ Film. The Interface Between the First (Figure 16) and Second Films is Found to be at Channel No. 278 by Comparison to Figure 17	65
19	RBS Spectrum of the Sample in Figure 18 After a 30-Minute Anneal at 850°C. Note, the Shift in the Main Ga Peak to the Interface (IF) and the Appearance of a Ga Peak at the Surface	68
20	RBS Spectrum of the Sample in Figure 18 After a 4 1/2 Hour Anneal at 850°C	68
21	Relative Amounts of Ga Observed in the RBS Spectra Before Annealing and After Each Anneal at 850°C up to 4 1/2 Hours. The TIC (Total Integrated Count) Is Proportional to the Total Amount of Ga Present. The (.) Symbols Are for the Data of this Section (Table 1) and the (X) Symbols for the Data of Section V 4.b (Table 2)	71
22	RBS Spectrum of a Ga - Pb Implant into a $SiO_2$ Film on Si, Over-coated with $SiO_2$	76
23	RBS Spectrum of a GaP Crystal Implanted with Zn to a Dose of $10^{16}/cm^2$ , Coated with $SiO_2$ , and Annealed for 85 Minutes at 850°C. Note that Ga and P Are at the Surface But Si is Shifted Back, Indicating a GaP Surface Film	80



LIST OF ILLUSTRATIONS (Cont'd)

FIGURE		PAGE
24	RBS Spectrum of the Sample of Figure 23 Coated Again with $\text{SiO}_2$ and Annealed for an Additional 90 Minutes at $850^\circ\text{C}$ . Again, Note the Presence of Ga and P at the Surface Indicating a New GaP Surface Film	80

SECTION I  
INTRODUCTION

Rutherford Backscattering offers a powerful tool for probing the surface regions of solid state materials and thin films. The method consists of using a beam of high energy (1-2 MeV) low mass (generally He) particles as a probe and analyzing the energy spectrum of the fraction that is backscattered through a large angle, 160-170°. The probe ions suffer elastic collisions with the target atoms and additionally suffer a continuous energy loss as they move through the lattice, both before and after the elastic collision. The rate of energy loss or "stopping power" is a function of the lattice or target ions, the probe ions, and the energy of the probe ions. The backscattered ions are collected at a fixed angle and their number as a function of energy is measured using a solid state detector and multichannel analyzer. The resulting spectrum is the output data for the measurement and contains information about the mass of the atoms in the target as well as their numbers and spatial location relative to the surface. One of the advantages of the RBS technique is that each scattering event is independent so that the spectrum is dependent only upon the numbers, mass, and locations of the atoms composing the target, which greatly simplifies analysis. However, this advantage is also a weakness in some cases because the spectrum contains no information about how the constituent atoms are combined, if at all. For example, when examining Ga in SiO<sub>2</sub> films as described later, it is not possible to comment on whether or not any of the oxygen is combined with the Ga. The fraction of the probe ions that are backscattered can be dramatically reduced if the probe beam is aimed along a low index direction in a single crystal



target, i.e., channeled. Channeling, in some applications, aids in extracting data, particularly in the cases of dopant ions located at specific lattice sites in single crystals and amorphous films on single crystal substrates which are discussed by Mayer et al. (Reference 1) and Mayer (Reference 2), respectively.

The primary purpose of this report is to review, examine, and apply the RBS (Rutherford Backscattering) technique to evaluating passivating films on semiconductors. Such films are used routinely to protect semiconductor surfaces during annealing, and therefore play a central role in the final properties of the material as shown, for example, by Harris et al. (Reference 3) and Feldman et al. (Reference 4) in the cases of GaAs and GaP, respectively. In addition, other applications of RBS for surface analysis are discussed and employed in an effort to demonstrate to some degree the technique's potential.



## RUTHERFORD BACKSCATTERING

## 1. GENERAL

Rutherford type scattering consists of projectiles striking target atoms with an energy sufficiently large to prevent any significant screening by the electrons on the projectile or target atoms. That is, Rutherford scattering consists of elastic binary scattering between the "bare" projectile and target nuclei which therefore "sense" only  $1/r^2$  type coulomb repulsion when they are a distance  $r$  apart. This sort of scattering permits greatly simplified quantitative interpretation of the data, which is aided further by using a monoenergetic source for the projectile ions.

The Rutherford scattering probability in the center-of-mass coordinate system for a particle of mass  $M_1$ , charge  $Z_1$ , and energy  $E$ , to be scattered through angle  $\theta$  by a target atom of mass  $M_2$  and charge  $Z_2$  into a solid angle  $d\Omega$  is given by

$$\left(\frac{d\sigma}{d\Omega}\right)_{\text{c.m.}} = \left(\frac{Z_1 Z_2 e^2}{4E}\right)^2 \left(\frac{M_1 + M_2}{M_2}\right)^2 \frac{1}{\sin^4(\theta/2)} \quad (1)$$

where  $e$  is the electronic charge. Expressing  $E$  in MeV, Equation 1 is a small quantity with strong forward-peaking,

$$\left(\frac{d\sigma}{d\Omega}\right)_{\text{c.m.}} = 1.3 \times 10^{-27} \left(\frac{Z_1 Z_2}{E}\right)^2 \left(\frac{M_1 + M_2}{M_2}\right)^2 \frac{1}{\sin^4(\theta/2)} \frac{\text{cm}^2}{\text{Sr}} \quad (2)$$

which says basically that the impinging projectile ion "sees" a very open lattice and that only a small fraction of the impinging particles are in fact backscattered. It is assumed for purposes of analysis that the incident flux is constant with depth. This assumption greatly simplifies analysis since losses from the incident beam can be ignored when comparing backscatter yields from different depths. The particles which are scattered come from varying depths in the target depending upon where they happen to approach a lattice atom within its effective scattering radius of which the Thomas-Fermi screening distance is a useable estimate. The Thomas-Fermi screening distance is typically a small fraction of one  $\text{\AA}$  and is a function of both the probe and target ions as can be seen from the values given on p. 127 of Mayer et al. (Reference 1).

Shown in Figure 1 is a typical RBS spectrum for a "random" sample (or target) in which the number of backscattered particles (or yield) is plotted as a function of energy. The front (or high energy) edge,  $E_s$ , of the spectrum represents elastic scattering from surface atoms, while the yield at lower energies is the result of ions that have traveled into the sample some distance, undergone elastic collisions, then returned to the surface where their energy is measured. The continuous inelastic energy losses experienced by the projectile ions while traveling through the crystal before and after the Rutherford collision give rise to the spectrum nature of Figure 1. These losses, which result from the stopping power of the particular ion-target-energy combination, are known and can be used to convert the spectrum's energy scale to a



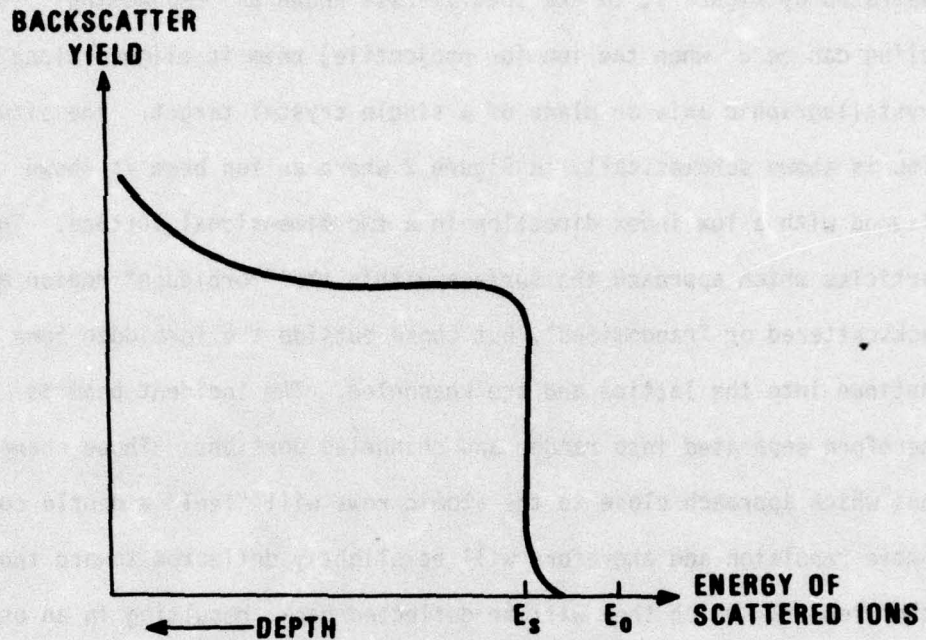


Figure 1. Schematic RBS (Rutherford Backscatter) Spectrum from a Random Sample.  $E_0$  and  $E_s$  Are the Energies of the Incident and Surface Scattered Ions, Respectively.

depth scale as indicated in Figure 1. The value of this conversion will be shown later when it is possible to track diffusing Ga in  $\text{SiO}_2$  and to locate its position relative to the specimen surface. Therefore, RBS can be viewed as a mass-sensitive depth microscope that permits mapping the location of masses to depths of a few  $\mu\text{m}$  with a resolution of up to  $\sim 30\text{\AA}$ .

A sample's backscatter yield can be greatly reduced, from that illustrated by Figure 1, in the special case known as "channeling". Channeling can occur when the ion (or projectile) beam is aligned along a crystallographic axis or plane of a single crystal target. The situation is shown schematically in Figure 2 where an ion beam is shown aligned with a low index direction in a two-dimensional lattice. Those particles which approach the surface within the "forbidden" region are backscattered or "randomized", but those outside the forbidden zone continue into the lattice and are channeled. The incident beam is therefore separated into random and channeled portions. Those channeled ions which approach close to the atomic rows will "feel" a gentle coulombic repulsion and therefore will be slightly deflected toward the other row from which they will be deflected back, resulting in an oscillating path leading deeper into the crystal (as indicated in Figure 2) with only gradual randomization or dechanneling. Thermal oscillations of the lattice atoms additionally contribute to the randomization process so that eventually most ions are dechanneled by approaching a lattice atom within the forbidden region, as discussed by Grasso (p. 181 of Reference 5).

To explore the channeling phenomena experimentally, a low index direction of the sample is carefully aligned with the ion beam and a backscatter spectrum is taken, which is shown schematically in Figure 3 superimposed on the random spectrum of Figure 1. The alignment is very critical since the angular difference between perfectly aligned and random spectra is typically a fraction of one degree. The surface peak in Figure 3 on the channeled curve results from the fraction of the ion beam that suffers Rutherford collisions with the surface atomic layer of



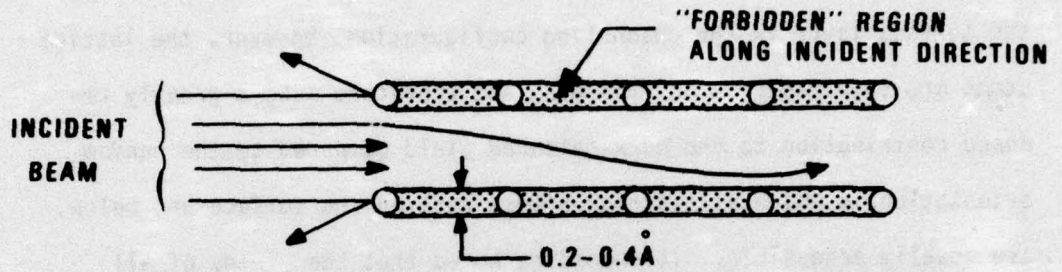


Figure 2. Illustration of an Incident Beam Parallel to a Low Index (Channeling) Direction in a Two-Dimensional Lattice.

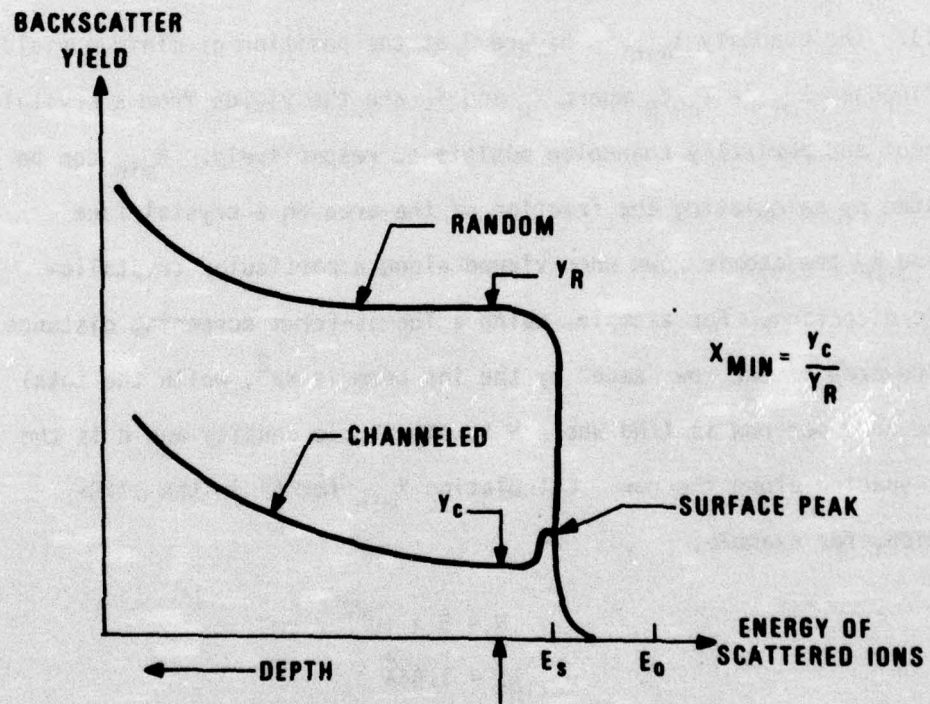


Figure 3. Schematic RBS Spectra for Channeled and Random Orientations of a Sample.  $E_0$  and  $E_s$  Are the Energies of the Incident and Surface Scattered Ions, Respectively.

the crystal as indicated in Figure 2. The surface contribution is the same from a crystal whether or not it is aligned for channeling. Beyond the surface layer in the channeling configuration, however, the lattice atoms are shielded from the ion beam and therefore make a greatly reduced contribution to the backscattered yield compared to the random orientation in which all lattice sites, both on the surface and below, are equally accessible. It should be noted that the yields of all backscatter spectra increase deeper in the crystal, (i.e. at lower energies in Figure 3) because the probe particle energy decreases as it penetrates the lattice due to the stopping power which results in an increased scattering cross-section or scattering probability (Equation 1). The quantity  $X_{\min}$  in Figure 3 at the position of minimum yield is defined as  $X_{\min} = Y_C/Y_R$  where  $Y_R$  and  $Y_C$  are the yields from a crystal in random and perfectly channeled positions, respectively.  $X_{\min}$  can be estimated by calculating the fraction of the area on a crystal face occupied by the atomic rows when viewed along a particular crystallographic direction. For example, using a Thomas-Fermi screening distance "a", the area of the row "seen" by the ion beam is  $\pi a^2$ , while the total surface area per row is  $1/Nd$  where  $N$  is the atomic density and  $d$  is the atomic spacing along the row. Calculating  $X_{\min}$  for Si in the  $\langle 110 \rangle$  direction, for example,

$$N = 5 \times 10^{22} / \text{cm}^3$$

$$d_{\langle 110 \rangle} = 3.84 \text{ \AA}$$

$$a = 0.17 \text{ \AA}$$

and

$$X_{\min} = \pi a^2 N d = 0.0174$$



This result means the lowest  $X_{\min}$  that can be obtained on a Si crystal regardless of surface preparation and alignment is about 2%, which is consistent with experimental observations.

More complete treatments of channeling, with examples, are available in publications by Picraux (Reference 6), Mayer et al. (Reference 1), and Morgan (Reference 5).

## 2. EXPERIMENTAL CONSIDERATIONS AND APPLICATIONS

The description of the RBS experiment given below is combined with discussions on the specific kinds of information that can be obtained about a material and how the experimental parameters interact with the measured data. Limitations of the RBS method are also discussed along with techniques by which some of them can be circumvented.

### a. Experimental Parameters

A typical experimental set-up for backscattering is shown schematically in Figure 4 where  $E_0$  is the incident ion energy and  $E$  is the ion's energy after scattering through the laboratory angle  $\phi$ . The sample is mounted on a goniometer so that the angle which the ion beam makes with the sample surface can be precisely adjusted over a wide range. When choosing how to perform the scattering experiment, consideration must be given to the available experimental parameters and how they affect the data that is required. The parameters consist of the probe ion energy, the angle of scattering, the method of detection, and the probe ion mass. It is assumed that all of the detected particles have undergone only a single close approach scattering event.

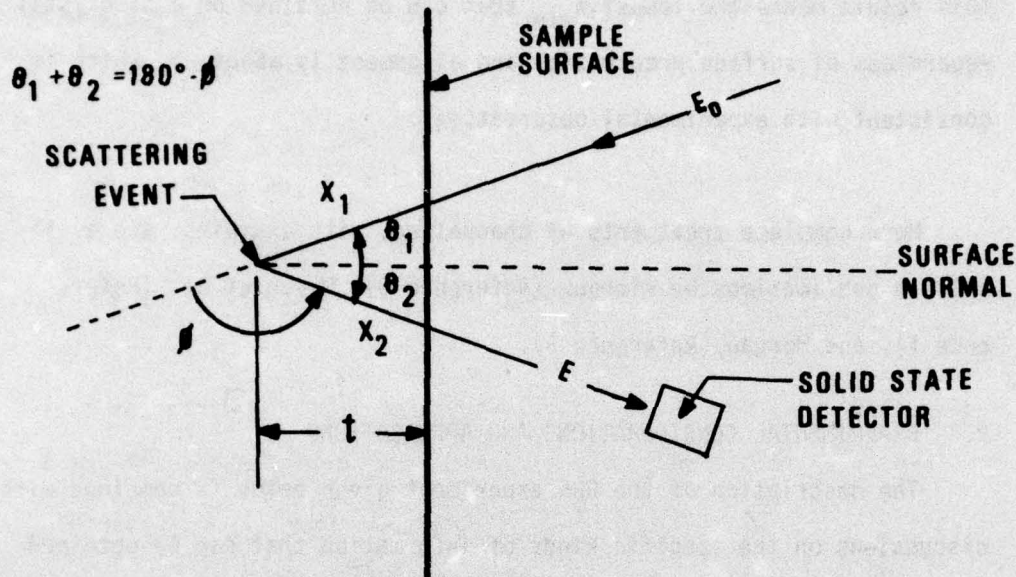


Figure 4. Typical Backscattering Set-Up for a Scattering Event at a Depth  $t$  in the Sample. Typically,  $\phi=168^\circ$  and  $\theta_1 + \theta_2=12^\circ$ .

The probe energy must be high for two primary reasons: (1) to improve the resolution between different masses in the target and (2) to ensure unscreened, binary collisions between the probe and target nuclei if the simplified data analysis advantage of Rutherford scattering is to be realized. Rutherford type collisions are further guaranteed by choosing a scattering angle  $\phi$  greater than  $90^\circ$ , and in fact as close to  $180^\circ$  as experimentally practical. This large value for  $\phi$  (typically  $168^\circ$ ) requires that the colliding particles approach with a small impact parameter which is defined as the perpendicular separation between the particles' center lines of motion before any deflection takes place due to the coulombic repulsive force. A small impact parameter combined



with the large incident energy ensures that any detected particle will have experienced a close-approach collision of the Rutherford type. Scattering dynamics are examined carefully by Carter and Colligon (Chapter 1 of Reference 7) and the classical Rutherford scattering theory is examined in some detail by Leighton (Chapter 14 of Reference 8). A small additional advantage of a large scattering angle is increased mass separation in the backscatter spectrum. That is, the energy difference between particles scattered from two different masses increases with scattering angle as can be seen from Equations 3 and 4. For example, the backscatter energy difference for He ions scattered from F and O at  $\phi = 145^\circ$  and  $175^\circ$  are, respectively

$$E(F) - E(O) = 64.9 \text{ keV}$$

and

$$E(F) - E(O) = 65.3 \text{ keV}$$

for an incident ion energy of 1 MeV. The major contribution to increased spectral separation of masses in the target is an increased energy of the incident ions. From Equation 3, it is seen that mass resolution is related linearly to the incident ion's energy, so the resolution is doubled in going from 1 MeV to 2 MeV.

Experimentally, the cost of scattering through a large angle with a large incident energy is a reduced number of scattering events because Equation 1 is forward peaked as mentioned and also because it decreases with increasing energy. Additionally, for backscattering the probe ion must be of a smaller mass than the target atom which can be seen from Equation 19 and is discussed by Armour and Carter (Reference 9).

The detector shown in Figure 4 is a solid-state Si, surface barrier type and is monitored by a multichannel analyzer. A scattered ion, upon entering the detector, creates an electronic pulse which is proportional in size to the particle's energy. This signal is amplified and stored in the multichannel analyzer according to its energy, so that all energies are continuously accepted by the detector while a scattering experiment is being performed. That is to say, a complete spectrum like that shown schematically in Figure 1 is obtained during a single run of perhaps 15-30 minutes while holding the sample at a fixed angle as it is struck continuously with a  $3 \times 10^{-9}$  ampere current of 2 MeV He ions. The convenience and efficiency of being able to accept all backscattered particles (within the solid angle of the detector) and to electronically discriminate between their energies, requires some compromises, namely, a reduced counting rate to avoid "pulse pile-up" and a reduced energy resolution. Pile-up occurs when two ions enter the detector within the time resolution of the electronics, then the two pulses add and appear as a single pulse with an energy equal to the sum of the two smaller pulses. Pile-up problems are minimized by using electronic pile-up rejection circuitry in addition to reduced ion currents. Solid state



detectors also have a limited energy resolution at room temperature of about 15 keV for  $\alpha$ -particles (He ions) in the 1-2 MeV range. In Si, this converts to a depth resolution of about  $300\text{\AA}$  at normal incidence, though a much better depth resolution is possible by using a low angle of incidence as described in Section II.2.e. In presently used sophisticated backscattering systems, the detector represents the basic resolution limitation. One notable exception is the apparatus developed by Bøgh (Reference 10) which uses a magnetic spectrometer and provides dramatically improved resolution for both mass and depth measurements. The major limitations of the magnetic analyzer, however, are the long time and large total ion dose required to obtain a single backscatter spectrum since the energy axis must be scanned and hence the count rate will necessarily be low for a narrow energy "window".

The final experimental parameter for consideration is the mass of the probe ions, which has a large effect upon the energy separation of the ions after being scattered from targets with different masses. That is, heavy probe ions (except for very light targets) result in a greater mass resolution than do lighter ions for the same initial energy, as shown graphically by Mayer, et al. (p. 142 of Reference 1). Unfortunately, the resolution of solid state detectors degrades with the probe ions of larger mass as shown by Bergström, et al. (Reference 11) (also p. 142 of Reference 1). In the case of carbon as a projectile, Chu et al. (Reference 12) show that no significant gain in resolution is achieved, though a real gain is realized in terms of reduced pile-up with both C

and N so that the sensitivity for heavy impurity detection is improved. Feldman et al. (Reference 4) show C to be useful for their specific need, i.e., examining low concentrations of shallow implants in GaP. However, for low mass targets, the mass sensitivity is decreased for increased probe ion mass and, in fact, backscattering is not possible for a probe mass equal to or greater than the target mass, as discussed previously. Heavy projectile ions also cause problems in terms of increasing the radiation damage in both the target and detector over that observed for He ions.

All factors considered,  ${}^4\text{He}$  is the best compromise for most experiments and is the ion used exclusively for the experiments described in this report. Typically, He ions (or  $\alpha$ -particles) with an energy of 2 MeV were used, and measured by a solid state detector at a scattering angle of  $168^\circ$ . These choices permitted seeing masses as low as  ${}^{12}\text{C}$  with ease, yet provided sufficient mass resolution and sensitivity for the heavy targets and impurities such as Hf and Au.

#### b. Scattering Depth

For elastic scattering, the energy before and after scattering are related by Equation 3

$$E = k^2 E_0 \quad (3)$$

where

$$k^2 = \left[ \frac{\beta \cos \phi + (1 - \beta^2 \sin^2 \phi)^{1/2}}{\beta + 1} \right]^2 \quad (4)$$



where

$$\beta = M_1/M_2$$

recalling that  $M_1$  is the projectile and  $M_2$  the target mass and that  $E_0$  and  $E$  are the incident and backscattered energies, respectively, of the probe particle. In Figure 3, Equation 4 permits calculation of the target mass,  $M_2$ , from the position of the front edge (or energy  $E_s$ ) of the spectrum when  $M_1$  and  $E_0$  are known. Determination of  $M_2$  is simplified with the use of Equation 5 which is an inversion of Equation 4:

$$\beta = \frac{1 - k^2}{1 + k^2 - 2k \cos\phi} \quad (5)$$

It is possible, with the aid of Figure 4, to work out the relationship between the energy of the backscattered particles and depth. The measured probe ion energy,  $E$ , at the detector results from stopping power losses before and after scattering in addition to a scattering (or  $k^2$ ) loss

$$E = k^2 \left[ E_0 - \int_0^{t/\cos\theta_1} \frac{dE}{dx_1} dx_1 \right] - \int_{\frac{t}{\cos\theta_2}}^0 \frac{dE}{dx_2} dx_2 \quad (6)$$

where  $\frac{dE}{dx_1}$  and  $\frac{dE}{dx_2}$  are the stopping powers for the particle going into the target and the particle coming back out after scattering. In the energy region used for this work, the stopping power relations are slowly varying functions as can be seen from the results of Northcliffe and Schilling (Reference 13). It is therefore practical for moderately thin layers (i.e. several thousand Å) to use average values for  $\frac{dE}{dx_1} = S(E_0)$  and  $\frac{dE}{dx_2} = S\left(k^2 \left[E_0 - tS(E_0)\right]\right)$  and to further approximate the energy during the  $\frac{dE}{dx_2}$  phase with  $k^2 E_0$ . Then Equation 6 becomes

$$E = k^2 \left[ E_0 - \frac{t}{\cos\theta_1} S(E_0) \right] - \frac{t}{\cos\theta_2} S(k^2 E_0)$$

which can then be solved for the depth at which the elastic collision occurs

$$t = \frac{k^2 E_0 - E}{\frac{k^2}{\cos\theta_1} S(E_0) + \frac{1}{\cos\theta_2} S(k^2 E_0)} \quad (7)$$

in the units of  $\mu\text{g}/\text{cm}^2$  when  $S$  is expressed in energy/ $\mu\text{g}/\text{cm}^2$ .

### c. Dopant Profile

The depth information contained in Equation 7 is of particular value when an impurity, such as an implanted layer, is present in the substrate. In such a case, if the impurity mass,  $M_i$ , is greater than the substrate mass,  $M_s$ , a RBS spectrum such as that shown in Figure 5 will be obtained where the impurity peak at  $E_i$  appears at a higher energy than the substrate edge,  $E_s$ . The impurity mass with the aid of



Equations 3 and 4 can be employed to calculate the scattered energy,  $k_i^2 E_0$ , to be anticipated if any impurity atoms were located on the surface. The difference  $k_i^2 E_0 - E_i$  is then the energy loss experienced by the probe in traveling through the lattice of the substrate to and from the implant. With the aid of Equation 7 and the stopping power and density of the lattice, the depth of the implant maximum and the profile with depth can be determined. These are the primary parameters that are required when implanting ions and are also the parameters that are tracked during annealing.

#### d. Thin Films

Another important (and often used) application of Equation 7 is for measuring the thickness of a passivating film deposited on a substrate. In this case, one obtains a RBS spectrum like that illustrated in Figure 6 for a silicon oxide film on a substrate with a mass greater than that of Si, which in turn has a mass greater than that of O. In Figure 6, the energy loss suffered by the probe particle traveling in through the film, colliding with a substrate atom at the interface, then traveling back out through the film is  $E_0 - E_S$ . Without the film, the energy loss of the ions would be  $E_0 - k_S^2 E_0$  so the additional energy loss due to the presence of the film is  $k_S^2 E_0 - E_S$  which when substituted into Equation 7 for  $k^2 E_0 - E$  yields a film thickness in cm if the stopping power and the density of the film are known.

In some circumstances, it is possible to determine the stoichiometry of the film by comparing relative yields of the film components with the aid of Equation 1 when expressed in the laboratory frame of reference. This point is discussed further in Section 3.

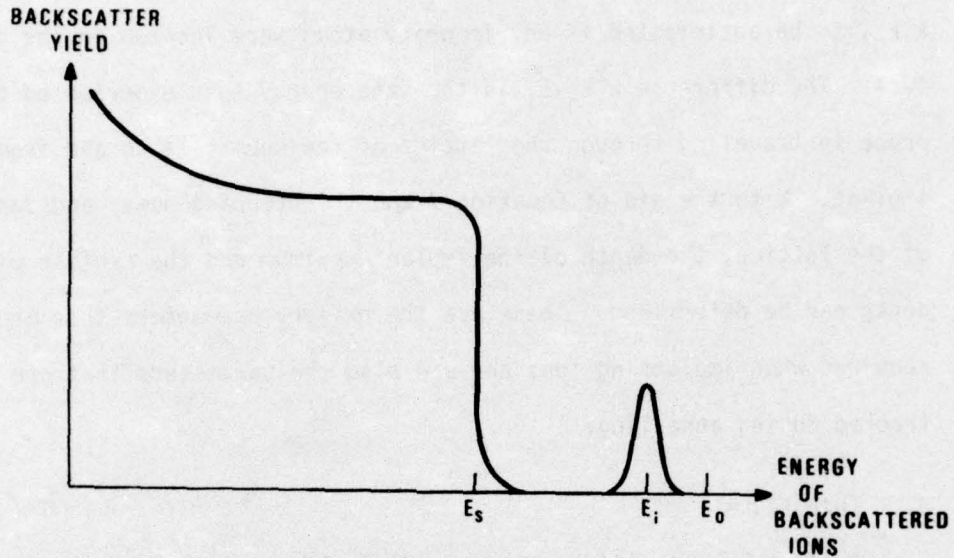


Figure 5. Schematic RBS Spectrum for an Impurity Layer (Mass= $M_i$ ) Near the Surface of a Substrate Material (Mass= $M_s$ ), Where  $M_i > M_s$ .  $E_0$  Is the Incident Energy of the Probe Beam.

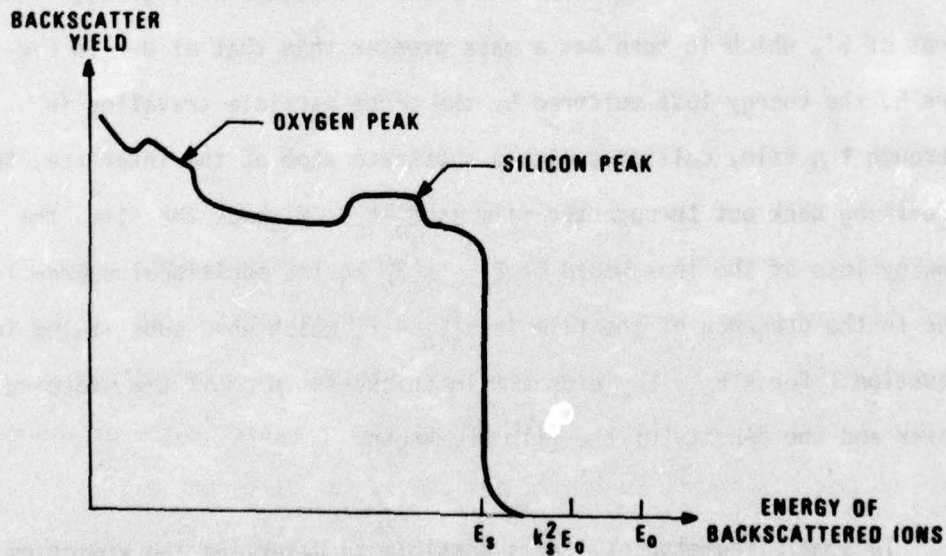


Figure 6. Schematic RBS Spectrum of a High Mass Substrate Coated with a Low Mass Silicon Oxide Film. The Energy  $k_s^2 E_0$  Represents the "Edge" Energy for Scattering from the Substrate with No Film Present and  $E_s$  Represents the Observed Edge Shifted Due to Stopping Power Losses of the Probe Particles As They Travel Into and Back Out Through the Film.



## e. Angle of Incidence

Not infrequently, an unknown impurity peak will appear in the spectrum and it is desired to know its mass. If in fact the impurity is at the surface of the sample, then with the aid of Equations 3, 4, and 5 the mass can be calculated since  $\phi$  is known for a given experiment and  $k^2$  is measured from the peak position. However, the peak position may be the result of mass and stopping power effects if the impurity is below the surface, a fact that can be definitely established by running backscatter spectra at more than one angle of incidence ( $\theta_1$  in Figure 4). This change in angle will change the path length and result in an energy shift of the impurity peak position due to stopping power effects if the impurity is below the surface and no shift if it is on the surface. For the case of the impurity located below the surface, an estimate of the path length (or depth in the sample), the stopping power losses, and finally, the impurity mass can be made by measuring the amount of shift observed between the two spectra.

Altering the angle of incidence of the probe particles ( $\theta_1$  in Figure 4) can also be used to permit a dramatic improvement in depth resolution over what is possible using the conventional "normal" incidence geometry ( $\theta_1 = 0$ ). The magnitude of this improvement can be roughly estimated by calculating the relative increase in the distance traveled by the projectile ion in the sample for different angles of

incidence. With the help of Figure 4, it is seen that for a scattering event at depth  $t$  the total path in the target =  $x_1 + x_2 = t (1/\cos\theta_1 + 1/\cos\theta_2)$ , so for  $\theta_1 = 0$  and  $\theta_2 = 12^\circ$

$$x_1 + x_2 = 2.02 t$$

while for  $\theta_1 = 80^\circ$  and  $\theta_2 = -68^\circ$

$$x_1 + x_2 = 8.43 t.$$

Therefore, the path length for  $\theta_1 = 80^\circ$  has increased by a factor of 4.17 over that for normal incidence. This increased path length improves the depth resolution of the measurement, because it means greater stopping power losses, and therefore a greater energy change, for an ion entering at  $\theta_1 = 80^\circ$  than for one entering at  $\theta_1 = 0$  even though both scatter at the same depth  $t$  below the surface. Present backscattering systems are limited primarily by the detector's energy resolution as discussed previously, so these increased energy losses experienced by the ion help solve the problem. The relation between depth resolution and detector resolution is seen directly by evaluating Equation 7 for scattering at two different depths  $t_1$  and  $t_2$ , then taking the difference:

$$t_1 - t_2 = \frac{E_2 - E_1}{\frac{k^2}{\cos\theta_1} S(E_0) + \frac{1}{\cos\theta_2} S(k^2 E_0)} \quad (8)$$



Taking  $\Delta E = E_2 - E_1$  as the detector's energy resolution, typically 15 keV FWHM (full width at half maximum), then  $\Delta t = t_1 - t_2$  represents the depth resolution. Rewriting Equation 8 for convenience,

$$\Delta t = \frac{\Delta E}{[S]} \quad (9)$$

where

$$[S] = \frac{k^2}{\cos\theta_1} S(E_0) + \frac{1}{\cos\theta_2} S(k^2 E_0) \quad (10)$$

and noting that for a given target  $[S]$  is a function of  $\theta_1$  and  $\theta_2$  while  $\Delta E$  is a constant for a particular detector, it is possible to calculate relative depth resolutions for changes in  $\theta_1$  and  $\theta_2$  as indicated in Equation 11

$$\Delta t (\theta_1 = \gamma) = \Delta t (\theta_1 = 0) \frac{[S (\theta_1 = 0)]}{[S (\theta_1 = \gamma)]} \quad (11)$$

recalling that  $\theta_1 + \theta_2 = 12^\circ$ . For example, if the scattering takes place with a very heavy target atom (i.e.  $\beta \approx 0$ ,  $k^2 \approx 1$ ) so that  $S(E_0) \approx S(k^2 E_0)$ , then Equation 11 gives for  $\gamma = 80^\circ$ ,

$$\Delta t (\theta_1 = 80^\circ) = \Delta t (\theta_1 = 0) \times \frac{1}{4.17}$$

which is the value found above using only the change in path lengths for the two angles of incidence. This result tells us that a given detector energy resolution corresponds to a smaller depth change in the target at glancing incidence than at normal incidence, so the resolution is increased accordingly, i.e. by 4.17 in this case for  $\theta_1 = 80^\circ$  and by 7.4 for  $\theta_1 = 85^\circ$ . In the case of real targets, the  $k^2$  and stopping power values are important, for example using 2 MeV  $\alpha$ -particles in  $\text{SiO}_2$ , the resolution improves in going from  $\theta_1 = 0$  to  $\theta_1 = 80^\circ$  by factors of 3.27 and 3.93 for scattering from oxygen and gallium, respectively.

As mentioned previously, another way to use the glancing incidence method, which is directly related to the earlier resolution discussion, is to change the "apparent" depth at which some particular scattering event occurs by changing the angle of incidence. Rewriting Equation 7 for scattering from depth  $t$ ,

$$t = \frac{k^2 E_0 - E_{\theta_1} = 0}{[S(\theta_1 = 0)]} \quad (12)$$

with  $\theta_1 = 0$ , and subtracting from a similar equation for scattering at the same depth  $t$  but with  $\theta_1 = \gamma$ , Equation 13 results,

$$\left( k^2 E_0 - E_{\theta_1 = \gamma} \right) = \left( k^2 E_0 - E_{\theta_1 = 0} \right) \frac{[S(\theta_1 = \gamma)]}{[S(\theta_1 = 0)]} \quad (13)$$



which gives the change in energy observed in the backscatter spectrum for the increased angle of incidence. The changed energy, and hence the increased apparent depth of scattering, is related to the normal depth by the same factors found above for the resolution increases, e.g. 3.97 for scattering from Ga in  $\text{SiO}_2$  with  $\theta_1 = 80^\circ$  and  $\theta_1 + \theta_2 = 12^\circ$ .

In addition to the resolution improvement and apparent depth change, the glancing incidence technique also permits detailed analysis of quite thin films that would normally be less than the detector resolution at normal incidence. In the case of compound films, the incident angle can be adjusted to yield a maximum apparent film thickness that still avoids overlap of the components. Some applications of the technique are illustrated in Sections IV.1, IV.2, V.3, and V.4.a where the examinations of several film types and thicknesses are described.

Unfortunately, this list of advantages realized by simply changing the angle of incidence is not free. When  $\theta_1$  is about  $70^\circ$  or larger, the experiment becomes far more sensitive to the ion beam divergence and detector acceptance angle which are functions of the experimental apparatus, more sensitive to small angle (multiple) scattering and energy straggling which are bulk effects in the sample, and far more sensitive to the sample's surface condition. All of these factors along with the detector resolution reduce the overall resolution of the measurement because they detract from the ideal experiment, which would consist of a particle of perfectly defined energy  $E_0$  entering a target sample at a perfectly defined angle, experiencing a smooth and continuous stopping

power slowing force, undergoing a single Rutherford collision, and traveling out again smoothly before detection at a precise energy and at the same precise angle into which it had been scattered. However, in a real experiment all of the above factors enter and reduce the observed resolution:

- 1) divergence in the ion beam before striking the target means in effect that the angle of incidence is not exactly defined,
- 2) a finite angle of acceptance at the detector means that the angle through which the detected ions have been backscattered is not exactly defined,
- 3) multiple scattering, which consists of many very low angle scattering events and increases with distance traveled in the target, can gradually alter the ion's direction and means reduced precision in defining the Rutherford scattering event,
- 4) energy straggling, which is energy spreading of an originally monoenergetic beam, is a product of the statistical nature of energy loss processes; like multiple scattering, it increases with distance traveled in the target and detracts from precisely defining the RBS event, and
- 5) surface roughness of the sample, if long-range impairs precisely defining the angle of incidence, and if short-range interferes with exactly locating the sample's surface.



These factors have been examined carefully by Williams (References 14, 15) and their relative effects have been evaluated and tested experimentally. Williams finds that experiments can be performed with a  $5^\circ$  angle of incidence ( $\theta_1 = 85^\circ$ ) and reasonable counting rates if care is taken with controlling the experimental parameters and with sample preparation. This  $5^\circ$  angle of incidence can result, for example, in a depth resolution of about  $50\text{\AA}$  (compared to about  $350\text{\AA}$  at normal incidence) for near-surface analysis of heavy atoms in Si. He experimentally demonstrates the practical operating ranges for the experiment:

- 1) an ion beam divergence of about  $0.05^\circ$ ,
- 2) a detector acceptance angle of about  $2-3^\circ$ ,
- 3) a bulk sample thickness of about  $500\text{\AA}$  in a light lattice (Al), about  $300\text{\AA}$  in Ge, and considerably less in heavy materials such as Au before a noticeable decrease in resolution is seen, and
- 4) a carefully prepared target surface such as that obtained by vibratory polishing and etching.

This technique for increasing the spatial resolution of RBS by means of a glancing angle of incidence is newly developed by Williams (References 15, 14) at the University of Salford and has been used extensively in obtaining the results on thin films described later in this report.

## 3. STOPPING POWER

The stopping power of a material (or target) is the energy loss experienced by a probe ion as it travels through that material. The amount of energy loss is dependent upon the number of target ions with which the probe ion interacts and therefore is generally expressed in energy loss per mass/area. In addition to being a function of the probe and target ions, the stopping power is also dependent upon the probe ion energy, but can be conveniently determined for most probe-target-energy combinations by means of the results given by Northcliffe and Schilling (Reference 13). Northcliffe and Schilling (Reference 13) present in graphical form the stopping powers for solid materials relative to Al (Figure 9 of Reference 13) as functions of  $E/m$  of the probe beam. Additionally, they present the stopping powers in Al of several ions (Figure 2 of Reference 13) also as functions of  $E/m$  and in units of  $\frac{\text{keV}}{\mu\text{g}/\text{cm}^2}$ . Combining these two numbers, the stopping power of the desired ion with a given energy can be calculated in a particular material. For example, for 2MeV  $\alpha$ -particles in Ga, Figure 9 of Reference 13 yields

$$\frac{(dE/dx)_{\text{Ga}}}{(dE/dx)_{\text{Al}}} = 0.62$$

at  $E/m = 0.5$ . From Figure 2 of Reference 13,

$$\frac{1}{z^2} \left( \frac{dE}{dx} \right)_{\text{Al}} = 0.25 \frac{\text{keV}}{\mu\text{g}/\text{cm}^2}$$



so

$$(dE/dx)_{Al} = 1.00$$

therefore:

$$(dE/dx)_{Ga} = 0.62 \frac{\text{keV}}{\mu\text{g}/\text{cm}^2}$$

To obtain the stopping power as a function of thickness, it is necessary to multiply by the density, which for Ga is

$$\rho_{Ga} = 5.91 \text{ g/cm}^3$$

which yields

$$(dE/dx)_{Ga} = 36.64 \text{ eV/\AA}$$

The stopping power of a compound can be obtained in a similar way by using Bragg's additivity rule as given by Northcliffe and Schilling (Reference 13, p. 244)

$$\frac{\left(\frac{dE}{dx}\right)_{\text{compound}}}{\left(\frac{dE}{dx}\right)_{Al}} = \frac{1}{M} \sum_i N_i A_i \left(\frac{dE}{dx}\right)_i \quad (14)$$

where  $(dE/dx)_i$  is the stopping power of the element with  $N_i$  atoms of weight  $A_i$  and  $M$  is the molecular weight. For example, for  $\text{SiO}_2$ ,

$$\frac{\left(\frac{dE}{dx}\right)_{\text{SiO}_2}}{\left(\frac{dE}{dx}\right)_{\text{Al}}} = \frac{1}{60} \left[ 28 \frac{\left(\frac{dE}{dx}\right)_{\text{Si}}}{\left(\frac{dE}{dx}\right)_{\text{Al}}} + 32 \frac{\left(\frac{dE}{dx}\right)_{\text{O}}}{\left(\frac{dE}{dx}\right)_{\text{Al}}} \right] \quad (15)$$

which yields, for  $\text{SiO}_2$  deposited on GaP being probed by 2MeV  $\alpha$ -particles, values of

$$S(E_0) = 1.077 \frac{\text{keV}}{\mu\text{g}/\text{cm}^2}$$

for the ingoing particles and

$$S(k^2 E_0) = 1.160 \frac{\text{keV}}{\mu\text{g}/\text{cm}^2}$$

for the particles reflected by Ga particles at the interface. These stopping powers yield values of 24.12 and 25.98 eV/Å, respectively for the incident and scattered  $\alpha$ -particles using an  $\text{SiO}_2$  density of 2.24 g/cm<sup>3</sup> as given by Chu et al. (Reference 16). This stopping power data can be used to calculate the thickness of the  $\text{SiO}_2$  film directly in Å by combining it with the shift in the position of the Ga edge,  $k^2 E_0 - E$  expressed in eV, in Equation 7.



Experimentally, the stopping power can be measured with quite good accuracy by using a marker (such as a heavy implant or thin evaporated layer) behind a known thickness  $t$  of the material for which  $S(E)$  is desired. For RBS from a heavy marker such as Au, the scattering loss is less than 10% so  $S(E_0) \approx S(k^2 E_0)$  and Equation 7 becomes,

$$S(E_0) = \frac{k^2 E_0 - E}{t \left( \frac{k^2}{\cos\theta_1} + \frac{1}{\cos\theta_2} \right)} \quad (16)$$

which represents a very good approximation for near-surface scattering. The angle of incidence can be varied to test the thickness range over which the  $S(E_0) = S(k^2 E_0)$  approximation is valid by changing the actual path length traveled by the ion.

Basically, Equation 16 represents the approach taken by Thompson and Mackintosh (Reference 17) to examine stopping powers as functions of energy in Si and SiO<sub>2</sub> and additionally to test Bragg's rule, Equation 14. They find that the measured values of  $S(E)$  for SiO<sub>2</sub> are higher than the values calculated using the Bragg rule for ion energies above 800 keV and differ by about 10% at 1.7MeV. They suggest that the stopping power is dependent upon the physical state of the atoms of which the compound is composed, noting that the oxygen stopping power values used for the calculations were taken from measurements on O<sub>2</sub> gas. The measurements made by Feng, et al. (Reference 18) to test the validity of Bragg's over the energy range of 0.5 to 2.25MeV find that it holds for three metal alloy systems and for two iron oxides within their experimental error.

They find a disagreement of 10-20% between the calculated and measured values for  $Al_2O_3$ , however, but believe that it could very likely be due to errors in the available data on Al. Therefore, it appears that the reliability of Bragg's rule is primarily a function of the input data, and consequently when performing experiments which are very sensitive to stopping power values the only safe route is to measure directly the specific systems being examined.

#### 4. LABORATORY COORDINATE SYSTEM

The differential scattering cross section  $d\sigma$  expressed in Equation 1 is given in the center-of-mass frame of reference as indicated. However, experiments are performed in the laboratory frame, so it is necessary to transform Equation 1 into the laboratory coordinate system. This conversion is particularly important for accurate checks of stoichiometry even though some workers have ignored all contributions except the  $Z^2$  ratios which avoids the inconvenience of transforming to the laboratory frame, but usually introduces considerable error.

Rewriting Equation 1

$$\left(\frac{d\sigma}{d\Omega}\right)_{c.m.} = \left(\frac{Z_1 Z_2 e^2}{2E}\right)^2 \frac{(B+1)^2}{4} \frac{1}{\sin^4\left(\frac{\theta}{2}\right)} \quad (17)$$



recalling that  $\beta = M_1/M_2$ . The center-of-mass angle  $\theta$  is related to the laboratory angle  $\phi$ , defined by Figure 4, by Equation 18 (see for example, Reference 9)

$$\tan \phi = \frac{\sin \theta}{\beta + \cos \theta} \quad (18)$$

from which the inverse relation can be derived (Equation 19):

$$\theta = \phi + \sin^{-1} (\beta \sin \phi) \quad (19)$$

It must be noted that the solid angle into which the particles are back-scattered

$$d\Omega_{\text{c.m.}} = 2\pi \sin \theta d\theta \quad (20)$$

must also be converted so that the differential scattering cross section becomes expressed completely in the laboratory angle  $\phi$ .

Substituting Equation 19 into Equations 17 and 20 and combining, Equation 21 results

$$\left(\frac{d\sigma}{d\Omega}\right)_{\text{Lab.}} = \left(\frac{Z_1 Z_2 e^2}{2E}\right)^2 \frac{1}{\sin^4 \phi} \cdot \frac{(\cos \phi + \{1 - \beta^2 \sin^2 \phi\}^{1/2})^2}{\{1 - \beta^2 \sin^2 \phi\}^{1/2}} \quad (21)$$

which is the form expressed in Reference 19 (which deleted the  $1/\sin^4 \phi$  term). In some cases it may be useful to express  $(d\sigma/d\Omega)_{\text{lab}}$  in center-of-mass angles, in which case it is readily shown that

$$d\Omega_{\text{Lab.}} = \frac{1 + \beta \cos \theta}{(1 + \beta^2 + 2\beta \cos \theta)^{3/2}} d\Omega_{\text{c.m.}} \quad (22)$$

so the scattering yield in the laboratory system is expressed by Equation 23

$$\left(\frac{d\sigma}{d\Omega}\right)_{\text{Lab.}} = \left(\frac{Z_1 Z_2 e^2}{2E}\right)^2 \frac{(\beta + 1)^2}{4} \cdot \frac{1}{\sin^4\left(\frac{\theta}{2}\right)} \cdot \frac{(1 + \beta^2 + 2\beta \cos\theta)^{3/2}}{(1 + \beta \cos\theta)} \quad (23)$$

This form is primarily of value when one is interested in evaluating the relative contributions of the different terms in stoichiometry calculations, which in the case of GaP shows that merely using the  $Z^2$  ratio

$$\left(Z_{\text{Ga}}/Z_{\text{P}}\right)^2 = 4.2711$$

while the correct ratio is significantly greater

$$\frac{(d\sigma/d\Omega)_{\text{Ga}}}{(d\sigma/d\Omega)_{\text{P}}} = 4.3731$$

at  $\phi = 150^\circ$ . However, when using the form of Equation 23, care must be exercised to use the correct angles, for example at  $\phi = 150^\circ$ ,  $\theta_{\text{Ga}} = 151.645^\circ$  and  $\theta_{\text{P}} = 153.705^\circ$  (Equation 19).



SECTION III  
IMPURITY DETECTION AND STOICHIOMETRY

## 1. GENERAL

The Rutherford backscattering technique offers a method by which the stoichiometry of compounds can, under favorable conditions, be measured to an accuracy of about a percent and the presence of impurities can be established generally to a fraction of one percent. This capability is of particular value when in the case of films deposited by different techniques it is necessary to know which method yields the desired ratio of components and whether or not impurities are introduced. RBS has also been employed to look at the introduction of impurities and compositional variations in the surfaces of compounds prepared with different etches. The ultimate accuracy is limited by geometric factors such as precise definition of the scattering angle and beam divergence, by counting statistics and background, by detector resolution, by multiple scattering and energy straggling, and by any deviations from the Rutherford scattering relation (Equation 21) which assumes no screening, an assumption that decreases in validity as the ion's energy is reduced. Using a sufficiently high ion beam energy (1-2MeV) and after exercising the experimental care described in Section II.2.e regarding low angle of incidence resolution improvements, sensitivity in measuring stoichiometry and detecting impurities is further improved by reducing the background and increasing the total count. The background reduction is approached in several ways, namely, by using a substrate of lower mass than the film and/or impurity, by examining light impurities in thin films, and by using channeling in single crystal substrates. All of these approaches are described below.

The method relies upon the fact that the Rutherford equation is a scattering probability so that the ratio of particles backscattered from each constituent of a compound is proportional to the number of each component present times the scattering probability as expressed in Equation 24

$$\frac{Y_A}{Y_B} = \frac{\left(\frac{d\sigma}{d\Omega}\right)_A}{\left(\frac{d\sigma}{d\Omega}\right)_B} \cdot \frac{N_A}{N_B} \quad (24)$$

where  $Y_A$  and  $Y_B$  are the scattered yields (number of backscattered particles) from components A and B and  $N_A$  and  $N_B$  are the number densities of each component. This same equation is used to calculate the concentration of implanted ions in which case the yield from the implant is compared to that of the substrate of which the number density is known and which allows the implant density to be calculated. Also, the concentration of impurities (in a substrate) can be estimated in a like manner.

## 2. SURFACES

Surface composition, principally stoichiometry, can be examined in some detail by employing channeling techniques and comparing the surface peaks (Figure 3) of the components. Hvalgård et al. (Reference 20) demonstrated how different etches resulted in dramatically different surfaces on their Te and Sn doped GaAs, and showed that some conditions yielded surfaces that were highly Te or Sn rich. Morgan and Bøgh (Reference 21) demonstrated in GaAs how the surface stoichiometry could be



adjusted and impurities introduced by the particular choice of etchant. Morgan and Wood (Reference 22) used the method to demonstrate its sensitivity in three systems, InP, GaAs, and GaP. In Reference 22 the general area of surface analysis is reviewed, experimental problems are discussed, and experimental data are presented for the three systems, in addition a summation is presented on the limitations of the technique both for evaluating the surface stoichiometry and probing for impurities.

It should be noted that since the best spatial resolution for Rutherford scattering is about 40-50 Å (Section II.2.e) and its probing depth is about one μm, RBS is not a surface tool in the same sense as is Auger spectroscopy, for example, which examines a few monolayers. That is to say, RBS can measure the presence of impurities and variations in stoichiometry within its resolution but a complimentary high resolution technique is required if greater depth sensitivity is necessary.

### 3. BULK COMPOUNDS

In general, the stoichiometry measurement is at best accurate to only about one percent under good, low background conditions which makes it of minimal value for any useable bulk semiconductor compound where the background level is high for at least one component. The sensitivity problems are discussed briefly by Carter and Whitton in Reference 23 for the case of GaP.

## 4. FILMS

Films of several types have been investigated in various ways to determine composition as a property of the film and as a function of depth. Also, they have been examined as a function of the growth properties both in terms of their stoichiometry and impurity content.

It is worth noting here that with RBS the composition of films can be calculated using experimentally measured quantities only without requiring external standards or needing to introduce stopping power terms, which are generally not known with a high degree of accuracy. (Further, the stopping power depends upon the composition which would introduce additional errors.) This point, which is summarized below and experimentally only requires a sharp interface between the film and substrate, is introduced and discussed by Meyer et al. (Reference 24) and is examined in detail by Chu et al. (Reference 12).

Figure 7 shows schematically the backscatter spectrum for a  $\text{SiO}_x$  film. The energy  $\Delta E_{\text{Si}}$  represents the energy difference between  $\alpha$ -particles scattered by Si atoms at the film surface and Si atoms at the back of the film where it interfaces the substrate, likewise,  $\Delta E_0$  is the energy difference for scattering from O atoms at the front and back of the film. In Equation 24, the yield can be expressed as the area under the peaks, so Equation 24 becomes

$$\frac{N_{\text{Si}}}{N_0} = \frac{\Delta E_{\text{Si}}}{\Delta E_0} \cdot \frac{H_{\text{Si}}}{H_0} \cdot \frac{\left(\frac{d\sigma}{d\Omega}\right)_0}{\left(\frac{d\sigma}{d\Omega}\right)_{\text{Si}}} \quad (25)$$



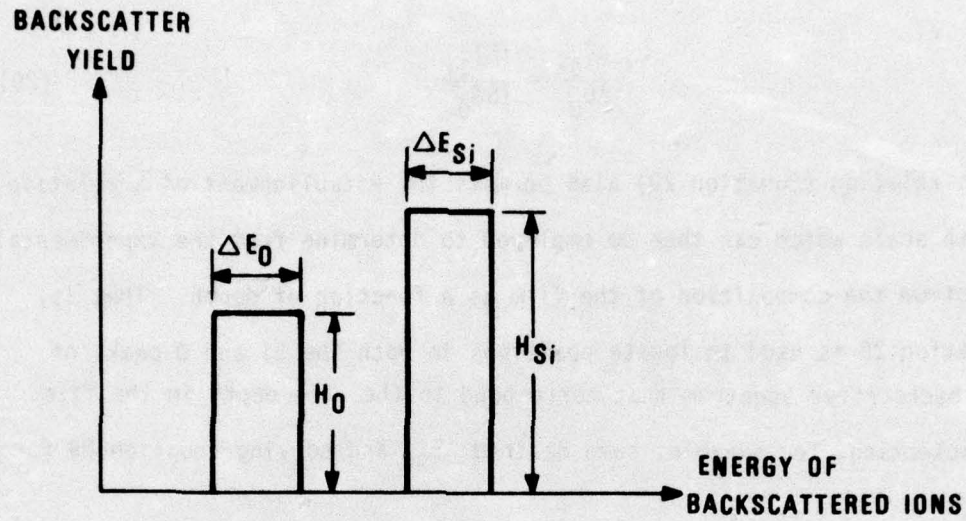


Figure 7. Schematic RBS Spectrum for an  $\text{SiO}_x$  Film.

for the ratio of the number densities and is expressed in terms of quantities directly determined from the spectrum. Also, the ratio of stopping power terms can be determined from the spectrum which is seen by rewriting Equation 7

$$\Delta E_{\text{Si}} = [S]_{\text{Si}} t \quad (26)$$

$$\Delta E_0 = [S]_0 t \quad (27)$$

where

$$[S]_{\text{Si}} = \frac{k_{\text{Si}}^2}{\cos^2 \theta_1} S(E_0) + \frac{1}{\cos^2 \theta_2} S(k_{\text{Si}}^2 E_0) \quad (28)$$

and likewise for  $[S]_0$ .

The ratio of Equations 26 and 27 yield Equation 29 for any depth  $t$ :

$$\frac{\Delta E_{Si}}{\Delta E_0} = \frac{[S]_{Si}}{[S]_0} \quad (29)$$

This relation (Equation 29) also permits the establishment of a relative depth scale which can then be employed to determine from the experimental spectrum the composition of the film as a function of depth. That is, Equation 29 is used to locate positions in both the Si and O peaks of the backscatter spectrum that correspond to the same depth in the film by selecting, for example, some desired  $\Delta E_{Si}$  and solving Equation 29 for  $\Delta E_0$ .

One of the major goals is to decrease the background in the spectrum in order to increase the sensitivity of these measurements. Some workers have approached this problem through the use of channeling methods and others through the employment of low mass substrates or free standing films. In general, RBS is used to examine heavy impurities in a light lattice, for example Ga in  $SiO_2$  which will be explored in Section V. It is also possible, however, to examine light impurities in a heavier lattice by using a thin film on a very light substrate. For example, the range and profile of Si implanted into Ge can be measured directly with RBS by depositing the Ge on a C substrate. In this case, if the Ge film thickness is chosen carefully, the Si peak in the RBS spectrum will appear between the back edge of the Ge film and the C edge of the substrate. The most dramatic demonstration of this approach has been given by Blewer (Reference 25) who examined He implanted into Cu by probing a free-standing film with protons of sufficient energy to enhance the He backscatter signal with a resonance.



The following subsections review some of the relevant work that has appeared in the literature examining passivating films, while Section IV uses experimental results to demonstrate the analysis of compound films prepared on low mass substrates by both RF sputtering and thermal evaporation.

Presently, some very useful review articles exist. For example, Morgan (Reference 26) discusses several types of films ( $\text{SiO}_x$ ,  $\text{Cu}_2\text{O}$ ,  $\text{CaF}_2$ , and  $\text{CdS}$ ) and suggests that RBS may be a method by which to locate the source of the erratic electrical behavior that has been observed in insulating films by many workers. He proposes that the electrical properties of the films are related to the composition and impurity content which can be determined from backscattering. Chu et al. (Reference 12) present a very extensive review of the application of ion beam analysis techniques to films and surfaces. They discuss several energy ranges including nuclear reaction analysis and comment on some of the practical experimental considerations. A short review by Mayer and Turos (Reference 27) compares RBS to some of the other experimental techniques for examining surface layers. Another article by Mayer et al. (Reference 28) briefly reviews the range of work carried out by the group at the California Institute of Technology looking at surfaces by the backscattering method and includes evaluation of oxides as well as diffusion of metals used for contacts. Finally, a review by Mayer (Reference 2) discusses the advantages and disadvantages of using channeling for semiconductor analysis and includes discussions on epitaxial layers, impurity atom location, alloying, and defects in compound as well as amorphous films.

a. Silicon Oxide - Literature Review

Technologically, silicon oxide is an important insulating film, and is used principally as a masking material in Si integrated circuits as well as a surface protective layer during the annealing of a variety of semiconductors including GaP as shown, for example, by Feldman et al. (Reference 4) and Hemenger and Dobbs (Reference 29). Also considerable literature exists on its electrical properties, see for example the review of Dearnaley et al. (Reference 30). In an effort to find correlation between its method of growth and electrical behavior, Morgan and Gittens (Reference 31) have examined  $\text{SiO}_x$  films prepared by different techniques using backscattering. Their primary contribution is preparing films on carbon substrates which dramatically reduces the background thus permitting stoichiometry measurements to an accuracy of about one percent and detection of impurity concentrations of approximately  $10^{18}/\text{cm}^3$ . They prepared films by evaporation, sputtering, thermal oxidation of Si, and ion implantation of O into Si. Related work on  $\text{SiO}_x$  and some other insulating films is discussed by Morgan in Reference 26.

Some early work by Meyer et al. (Reference 24) looked at relatively thick  $\text{SiO}_x$  films on Si prepared by thermal oxidation, anodizing, sputtering, and deposition from  $\text{SiH}_4$  and  $\text{O}_2$  using channeling to reduce the background. These investigators also introduced a line shape extraction method based upon channeling which has since been expanded. The results in Reference 24 indicated a variation in stoichiometry with thickness, but all the films were on average nearly  $\text{SiO}_2$ . More recent results by



Chu et al. (Reference 32) and Sigmon et al. (Reference 33) using a line shape extraction technique of increased sophistication also showed a strongly Si rich interface region for anodically and thermally grown very thin oxide films on Si. The method employed channeling to assist in carefully extracting the contribution made by Si in the film. The method used is based upon the technique introduced by Meyer et al. (Reference 24). It was carefully developed for examining  $Al_2O_3$  films on Si by Mitchell et al. (Reference 34) where it is described in great detail. Line shape extraction is required because of the overlap at the interface of the contributions to the spectrum from the Si (or Al) in the film and the Si in the substrate which hides the background and thus obscures the precise contribution to the spectrum from the Si (or Al) in the film alone. In spite of experimental difficulties, the results presented in References 32 and 33 are convincing due to the care taken in application of the method.

b. Silicon Nitride - Literature Review

Silicon nitride films are used as passivation layers on semiconductors and are possibly an improvement over silicon oxide for some applications, as discussed by Harris et al. (Reference 3), Chu et al. (Reference 35), as well as by Section V.2 of this report.

Films grown by deposition from  $SiH_4 + NH_3$  mixtures have been analyzed using RBS which has shown stoichiometry variations both overall and as functions of depth in the films when the silane to ammonia ratio

is varied as shown by Gyulai et al. (References 36, 37). These stoichiometry variations were correlated with measured changes in the density, dielectric constant, and index of refraction of the films. Films grown from silane and nitrogen have also been examined by Meyer and Scherber (Reference 38) using the backscattering method, in which case the stoichiometry of the films was found to vary with varying silane concentrations, but the density of the films tended to remain constant as well as the composition through the films' thickness. Reactively sputtered films of silicon nitride have been evaluated by Croset et al. (Reference 39) using a combination of the backscattering method and nuclear reactions. In these sputtered films, Ar was found distributed through the layers which were homogeneous, but which had a variable stoichiometry depending upon the  $N_2$  pressure during growth.

c. Aluminum Oxide - Literature Review

Aluminum oxide, like silicon oxide, is of value as a passivating and dielectric layer. Measurement of its stoichiometry by RBS, however, presents additional difficulty for films deposited on Si substrates because Al is a little more than one mass unit lighter than Si, a situation that leads to an overlap peak in the spectrum. The presence of the overlap peak requires that additional care be taken to correctly separate the contributions to the spectra from the film and the substrate. This peak profile extraction has in fact been accomplished convincingly using a channeling technique that is presented by Mitchell et al. (References 34, 40) who demonstrate the separation method using a free-standing film that is used first to generate the Al and O peaks without



any backing, then again with a Si crystal backing and application of the channeling extraction technique. The Al and O profiles obtained from the two measurements show excellent agreement and show the films to be stoichiometric. Reference 34 also looks at the stoichiometry, density, and Cl content of films deposited hydrolytically on Si substrates at different growth temperatures. Kamoshida et al. (References 41, 42) examine other properties of hydrolytically grown  $Al_2O_3$  films, in particular the effects of various anneals upon the films' final structure which is examined as a function of depth.

d. Native Oxides on III-V Semiconductors - Literature Review

Oxides grown on GaP both with and without an external anodic voltage have been examined by Poate et al. (Reference 43) for their chemical composition using Rutherford backscattering. A difference in both the stoichiometry and oxygen content were found for films produced by the two methods, in particular a Ga-rich layer was present near the surface of the specimens grown with an applied voltage, while the films grown without the applied voltage showed a uniform composition. Further work by Poate et al. (References 44, 45) on films grown on GaP crystals in solutions with various pH values also demonstrated films with uniform and variable compositions using, like Reference 43, the analysis described by Mitchell et al. (Reference 34). This later work showed that the films' average Ga/P ratio varies, being most nearly stoichiometric in the films that were least uniform in composition, i.e. had a Ga build-up near the surface.

Anodic films grown on GaAs have been examined using a combination of RBS and ion-induced x-rays as reported by Feldman et al. (Reference 46). In this case the backscattering method alone provides an oxygen to Ga and As ratio and only an indication of the distribution of Ga and As through the film because Ga and As are so close in mass. The increased mass resolution provided by ion-induced x-rays measured at glancing incidence, when used in conjunction with the RBS results, helps establish the ratio of the components throughout the film's thickness.



SECTION IV

ANALYSIS OF COMPOUND FILMS-EXPERIMENTAL RESULTS

1. SPUTTERED SILICON OXIDE-COMPOSITION

Films which are deposited using RF sputtering from a quartz ( $\text{SiO}_2$ ) source are commonly used to coat specimens for surface protection during annealing treatments, and it was films of this type that were employed for the experiments described in Section V. Therefore, it was necessary to know the films' properties, and primarily the composition to see if in fact  $\text{SiO}_2$  was being deposited.

The films were prepared in an Ar pressure of about  $70\mu\text{m}$  using a 13.5MHz source and a deposition rate of about  $0.5\text{\AA}/\text{sec}$ . For the measurements described in this section, it was decided that deposition on a vitreous carbon substrate would be the best approach. This technique, as demonstrated by Morgan and Gittens (Reference 31), does not require channeling for analysis as would be necessary for a film on Si, but still reduces the background significantly. Also, it is more feasible to use the glancing incidence method described by Williams (References 14, 15) with a carbon substrate which places no restrictions upon the analysis angle, restrictions that are present when channeling is required.

Shown in Figure 8 is the backscatter data from a silicon oxide film deposited by RF sputtering onto a polished vitreous carbon substrate. The experimental arrangement is shown schematically in Figure 9 which is Figure 4 modified to fit this particular case. A 50° angle of incidence was used because it maximized the apparent thickness of the film and hence the resolution but still avoided overlap of the oxygen and silicon components. This angle was varied experimentally to arrive at the 50° setting, and demonstrates the value of this additional parameter that becomes available when using the glancing incidence technique.

The data presented in Figure 8 was taken using 2MeV  $\alpha$ -particles and was collected in a multichannel analyzer set at 5keV/channel. Using Equation 4 for Si and O,

$$k_{Si}^2 = 0.5668128$$

and

$$k_O^2 = 0.3636936$$

which can be used with Equation 3 to calculate the expected positions of the Si and O edges in the spectrum,

$$\begin{aligned} E_{Si} &= 2 \times 10^6 \times 0.5668128 \\ &= 1.1336256 \times 10^6 \text{ eV} \end{aligned}$$



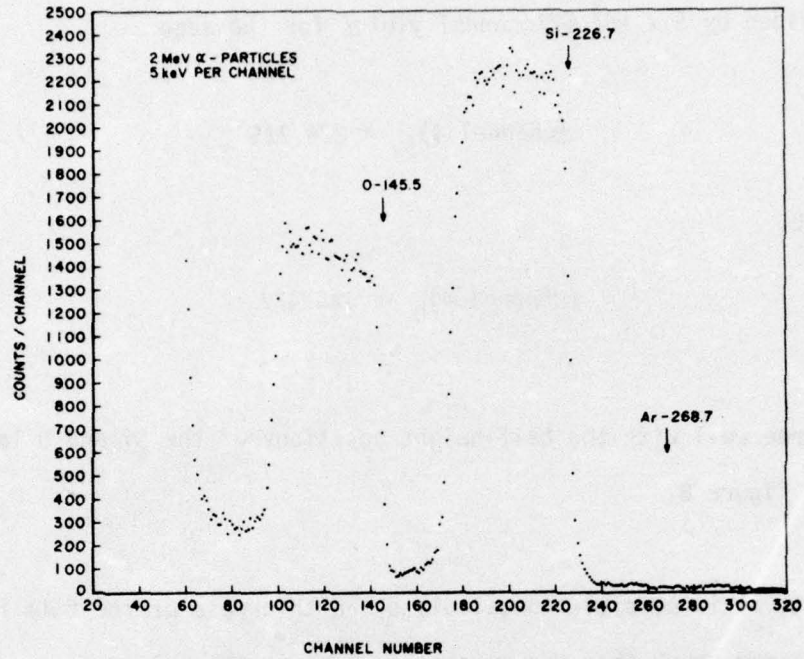


Figure 8. Backscatter Spectrum from a Silicon Oxide Film on a Carbon Substrate. Channel 226.7 Represents Scattering from Si on the Surface of the Film and Channel 175 from Si at the Si-C Interface, Likewise for O.

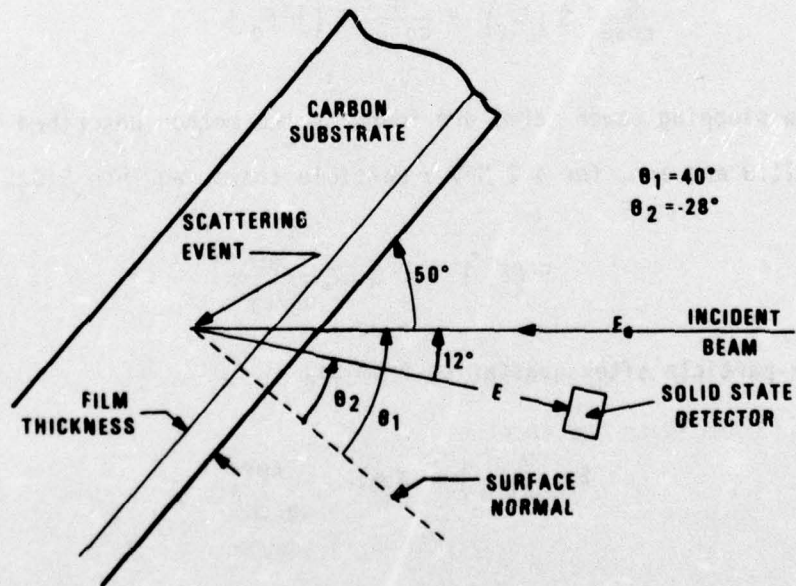


Figure 9. Experimental Arrangement Used for Collecting the RBS Data Shown in Figure 8.

AFML-TR-75-55

when divided by  $5 \times 10^3$  eV/channel yields for the edge

$$(\text{channel \#})_{\text{Si}} = 226.725$$

and for O,

$$(\text{channel \#})_{\text{O}} = 145.477$$

which agree well with the half-height positions of the Si and O leading edges in Figure 8.

Next, it is possible to calculate the thickness of the film from each peak and check them for agreement using Equation 7,

$$t = \frac{k^2 E_0 - E}{\frac{k^2}{\cos\theta_1} S(E_0) + \frac{1}{\cos\theta_2} S(k^2 E_0)} \quad (7)$$

where the stopping power terms are found by the method described in Section II.3 and are, for a 2 MeV  $\alpha$ -particle traveling into  $\text{SiO}_2$ ,

$$S(E_0) = 1.0767 \frac{\text{keV}}{\mu\text{g}/\text{cm}^2}$$

for the  $\alpha$ -particle after scattering from Si,

$$S(k_{\text{Si}}^2 E_0) = 1.3168 \frac{\text{keV}}{\mu\text{g}/\text{cm}^2}$$



and after scattering from 0,

$$S(k_0^2 E_0) = 1.4461 \frac{\text{keV}}{\mu\text{g}/\text{cm}^2}$$

For Si, the width of the peak is  $(227-175) = 52$  channels which at 5 keV/channel gives  $2.6 \times 10^5$  eV and is substituted for  $(k_{\text{Si}}^2 E_0 - E)$  in Equation 7

$$t_{\text{Si}} = \frac{2.6 \times 10^5}{\frac{k_{\text{Si}}^2}{\cos 40} S(E_0) + \frac{1}{\cos(-28)} S(k_{\text{Si}}^2 E_0)}$$

$$t_{\text{Si}} = 1.136 \times 10^{-4} \text{ g}/\text{cm}^2$$

which becomes, when expressed in  $\text{\AA}$ , for a bulk density of  $2.24 \text{ g}/\text{cm}^3$  (Reference 16)

$$(t/\rho)_{\text{Si}} = 5073 \text{ \AA} \quad (30)$$

and for the oxygen peak in Figure 8

$$t_0 = 1.09 \times 10^{-4} \text{ g}/\text{cm}^3$$

and

$$(t/\rho)_0 = 4881 \text{ \AA} \quad (31)$$

which agree in thickness to better than 4%. The difference most likely arises from errors in the stopping power functions because the ratios of  $\Delta E_{\text{Si}}/\Delta E_0$  (Equation 29) measured from the spectrum of Figure 8 and calculated from [S] values show a similar disagreement.

To calculate the stoichiometry of the film, Equations 24 and 21 are needed. For this case,

$$\frac{\left(\frac{d\sigma}{d\Omega}\right)_0}{\left(\frac{d\sigma}{d\Omega}\right)_{Si}} = \left(\frac{Z_0}{Z_{Si}}\right)^2 \frac{\left(\cos\phi + \left\{1 - \beta_0^2 \sin^2\phi\right\}^{1/2}\right)^2 \left\{1 - \beta_{Si}^2 \sin^2\phi\right\}^{1/2}}{\left(\cos\phi + \left\{1 - \beta_{Si}^2 \sin^2\phi\right\}^{1/2}\right)^2 \left\{1 - \beta_0^2 \sin^2\phi\right\}^{1/2}} \quad (32)$$

where  $Z_0 = 8$ ,  $Z_{Si} = 14$ ,  $\beta_0 = 4.0026/15.9994$ ,  $\beta_{Si} = 4.0026/28.086$  and  $\phi = 168^\circ$ . The yields  $Y_0$  and  $Y_{Si}$ , which are taken as the respective areas of the profiles, result after substitution into Equation 24 in an O/Si ratio of

$$N_0/N_{Si} = 1.858 \quad (33)$$

which indicates that the film is somewhat Si-rich. A measurement taken near the edge of the film gave a similar  $N_0/N_{Si}$  ratio, therefore the film's composition is uniform over the surface, which is expected.

By looking at Figure 8, it is clear that no impurities are present in large concentration. For example, a slight rise in the data is seen in the vicinity of channel #290, which is found to correspond to a mass of about 50 through the use of Equations 3 and 5. The concentration of this impurity compared to the concentration of Si atoms is found through the use of Equation 24 to be about 0.33%, which indicates the detection limit for this particular experiment. This sensitivity limit could be reduced by making a longer backscatter run, thus improving the statistics. It is worth noting that no measurable Ar appears in the film in spite of the fact that the film was sputtered in an Ar atmosphere. The position of the Ar edge is indicated in Figure 8.



## 2. OTHER FILMS - COMPOSITIONS AND IMPURITIES

While pursuing the main program, i.e. exploring the behavior of Ga in  $\text{SiO}_2$  films, opportunities arose during development of the technique that called for its application to some other systems which demonstrated important characteristics of the RBS method while simultaneously answering some immediate problems. The results of three such investigations are described below.

### a. Aluminum Fluoride

$\text{AlF}_x$  is an easily evaporated dielectric material which is being examined as a possible alternative to  $\text{SiO}_2$ . Some  $\text{AlF}_x$  films, grown by thermal evaporation from a powder, showed erratic electrical behavior and a stoichiometry problem was suspected. To determine whether or not this was a valid assumption, a film was prepared on a polished C substrate and a RBS spectrum was taken at normal incidence which is shown in Figure 10. In Figure 10, several features are immediately apparent:

- (1) the "wings" on the F peak indicate a composition variation with depth, with increased F concentrations at the interface and at the surface (at the start and finish of the evaporation),
- (2) a heavy impurity, probably Au as indicated, is present through the film,

- (3) an unknown impurity is present which gives rise to a small peak near channel 233.5, its mass (if assumed to be on the surface) falls between Si (channel 226.7) and P (channel 239.2) so it must be located within the film,
- (4) no other significant concentrations of impurities are visible.

The composition of the film is calculated using Equation 24 where the areas under the F and Al contributions are taken as the respective yields:

$$N_F/N_{Al} = 3.16$$

A stoichiometric film would be  $AlF_3$  so the film in Figure 10 is slightly F-rich, a not surprising result in view of the visible F wings. The heavy impurity which is assumed to be Au was found from the spectrum to have a number density of about  $3.1 \times 10^{19}/cm^3$  which is approximately 0.14% of the Al number density. This concentration would be sufficient to affect the dielectric properties of the film and is most likely the cause of the observed problems rather than is the stoichiometry.

The starting powder was suspected of being the source of the Au, so the RBS spectrum shown in Figure 11 was taken using as the target a pellet compressed from the powder to see if in fact the Au was present. Figure 11 shows no trace of Au within the sensitivity of the method which indicates that the impurity is introduced during evaporation (note



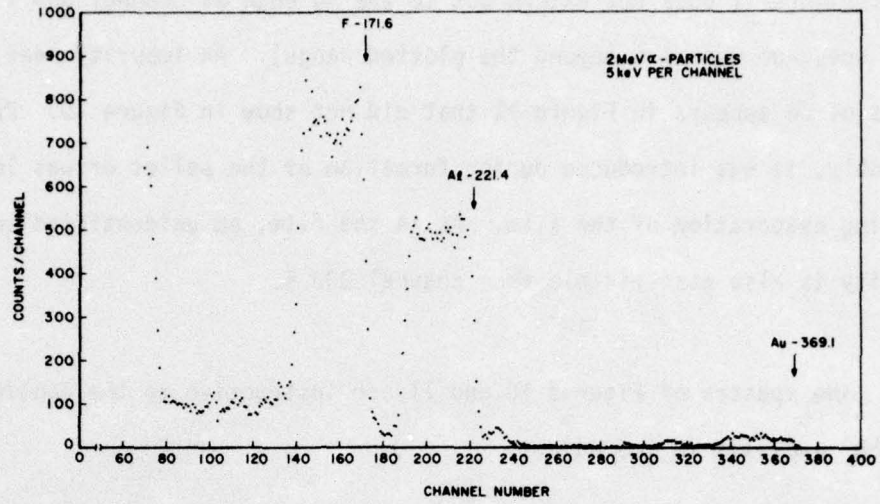


Figure 10. RBS Specimen from an  $\text{AlF}_x$  Film on a Carbon Substrate.

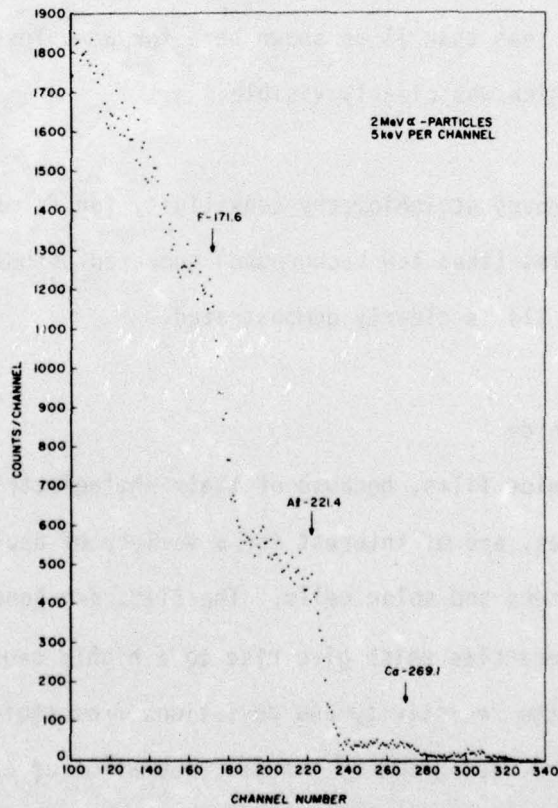


Figure 11. RBS Spectrum of an  $\text{AlF}_x$  Pellet. This Specimen Was Compressed from the Powder Used to Evaporate the Film Examined in Figure 10.

that Figure 11 does not extend out to the Au edge at channel 369.1 since the spectrum was zero beyond the plotted range). An impurity near the mass of Ca appears in Figure 11 that did not show in Figure 10. Presumably, it was introduced during formation of the pellet or was lost during evaporation of the film. As in the film, an unidentified impurity is also just visible near channel 233.5.

The spectra of Figures 10 and 11 are instructive to the application of RBS analysis in two ways:

- (1) the sensitivity to the presence of heavy impurities (large  $Z^2$ ) is much less than 1% as shown here for a Au level of about 0.14% which was clearly visible.
- (2) the improved stoichiometry sensitivity for films on low mass substrates (thus low background) compared to bulk samples (Figure 11) is clearly demonstrated.

b. Cadmium Selenide

Cadmium selenide films, because of their photoelectric and piezoelectric properties, are of interest for a variety of applications including transducers and solar cells. The films are generally n-type due to selenium vacancies which give rise to a highly sensitive relationship between the resistivity and deviations from stoichiometry. The films examined here were grown by vacuum evaporation of a CdSe powder with deposition onto polished Si substrates (Si was chosen for the substrate because of its low mass relative to Cd and Se). The final



composition of the films grown in this way is a function of the substrate temperature, deposition rate, and source temperature. The RBS technique was chosen as one way in which the relationships between growth conditions and film composition could possibly be established while simultaneously checking the films' purity.

Two CdSe films were prepared at the two extremes of the available deposition rates on Si substrates. Figure 12 shows a RBS spectrum for one of the films obtained with the probe beam at normal incidence to the surface ( $\theta_1 = 0$  in Figure 4). From Figure 12, the thickness is found to be nearly  $1000\text{\AA}$ , and the composition using Equation 24 is

$$N_{\text{Se}}/N_{\text{Cd}} = 1.04$$

which is several percent greater than the value measured for the other film grown at a different rate. Also of interest in Figure 12 is an impurity peak near channel 370, a peak which did not appear in the spectrum for the other film. To determine the location of the impurity relative to the surface of the sample, another RBS spectrum was taken at a  $30^\circ$  angle of incidence and is shown in Figure 13. It is noted that the surface peak position has not moved significantly between Figures 12 and 13, thus the impurity is located on the surface of the film. Further, the impurity peaks' width is still within the detector resolution (3-4 channels) which indicates a very thin layer. The particular impurity has a mass near that of Au, Pb, or Bi as indicated in Figure 12.

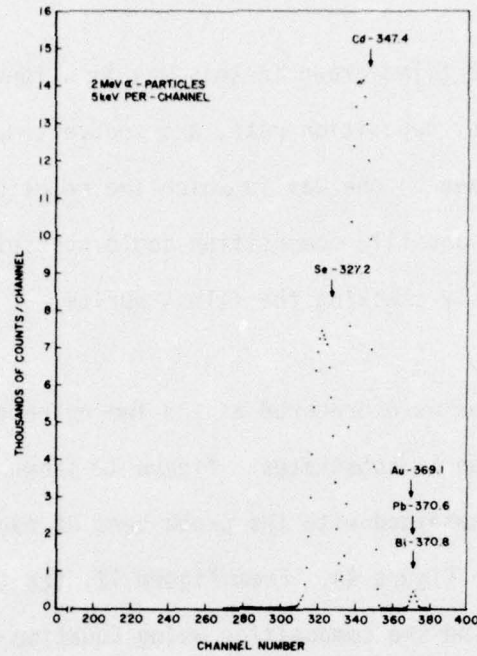


Figure 12. RBS Spectrum of a CdSe Film on a Si Substrate with a Heavy Impurity Near Channel No. 370. The Angle of Incidence is  $90^\circ$  ( $\theta_1=0$ ).

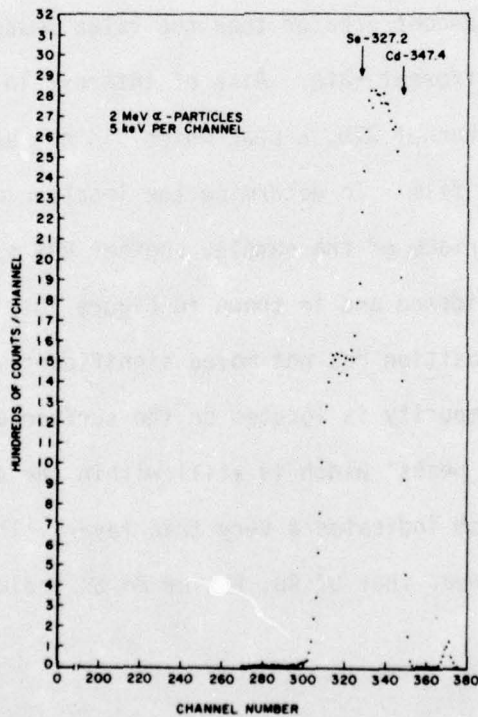


Figure 13. RBS Spectrum of the Sample Shown in Figure 12, but with a  $30^\circ$  Angle of Incidence ( $\theta_1=60^\circ$ ).



In Figure 13, note also that due to increased spatial resolution at the decreased angle of incidence, the CdSe film appears thicker thus the Cd and Se components overlap.

c. Hafnium Oxide

Insulating dielectric layers of hafnium dioxide are being examined for potential use in thin film capacitors. The films can be prepared by several approaches, for example sputtering, evaporation of Hf in an oxidizing atmosphere, or oxidation of Hf layers, and RBS appears to be an ideal tool for selecting the most promising materials. The RBS results described below were taken on a sample prepared by first vacuum depositing Hf onto a C substrate then baking the film in  $O_2$ . RBS spectra were taken in order to determine if the film was stoichiometric and to identify the types and concentrations of the impurities.

The RBS spectrum shown in Figure 14 was made with the probe beam at an angle of  $30^\circ$  to the surface. Unfortunately, due to a rather rough C substrate, a lower angle of incidence led to a long Hf tail and was thus not useable. In spite of rather poor statistics for the O peak, the composition ratio for O/Hf was measured and found to be greater than two. Therefore, adequate O is present to form  $HfO_2$  which was of primary concern. Further, within the experimental accuracy, the oxygen is distributed uniformly through the film, and no significant concentration of impurities is observed anywhere in the spectrum.

This system illustrates a weakness of the RBS method, i.e. where the components are greatly different in mass (and therefore  $Z^2$  values)

greater care must be taken to obtain meaningful data. In this case, a C substrate that was carefully polished, an increased running time of the RBS spectrum, and a thicker film would have contributed dramatically to an improved spectrum which could then have been optimized by adjusting the angle of incidence.

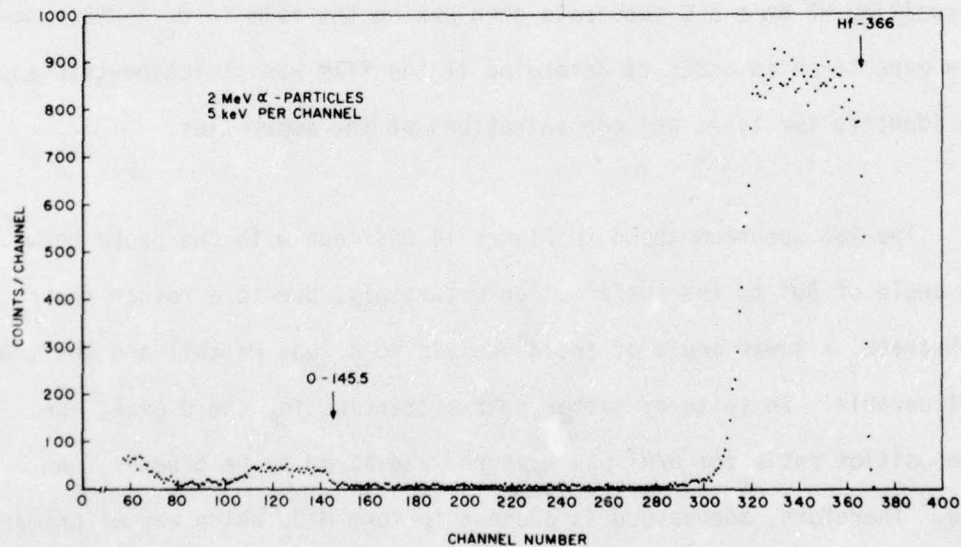


Figure 14. RBS Spectrum of a  $HfO_x$  Film on a Carbon Substrate ( $\theta_1=60^\circ$ ).



## SECTION V

## DIFFUSION OF GALLIUM IN ENCAPSULATING FILMS

## 1. GENERAL

Insulating films such as  $\text{SiO}_2$  and  $\text{Si}_3\text{N}_4$  are commonly used as passivating or protective layers on semiconductors to protect the surface during processing. For example, Feldman et al. (Reference 4) as well as Hemenger and Dobbs (Reference 29) have used  $\text{SiO}_2$  on GaP after implantation to guard against decomposition of the crystal during annealing at temperatures up to  $900^\circ\text{C}$ . In Reference 29 the p-layer depth after implanting with Zn, coating with sputtered  $\text{SiO}_2$ , and annealing for 1/2 hour at  $900^\circ\text{C}$  was estimated to be about  $10\mu\text{m}$  or less. Later results by Dobbs and Hemenger (Reference 47) with the scanning electron microscope, however, showed the p-layer thickness to be  $4\mu\text{m}$ . Further work (Reference 47) with a lower implant dose ( $10^{14}/\text{cm}^2$ ) showed similar behavior after a 1/2 hour anneal, and additionally showed a p-layer that increased in thickness with longer annealing times, a pattern that would presumably have been observed in the samples with the larger dose ( $10^{16}/\text{cm}^2$ ) if the annealing times had been extended. A maximum p-layer thickness of  $30\mu\text{m}$  was observed in the samples after annealing for 100 hours. The explanation for this p-layer that increased in thickness and in total number of p-type carriers with increasing anneal times must derive from some cause other than just the implanted Zn ions, because the total number of carriers exceeded the number of implanted ions after relatively short anneals. One model that seems feasible and explains the observed behavior is that Ga from the GaP lattice diffuses out through the  $\text{SiO}_2$  leaving behind Ga vacancies that behave as p-type defects. A literature search revealed evidence to support this model (see for

example the results found in GaAs by Harris et al. in Reference 3), but little work could be found that looked directly at the problem of Ga diffusion in silicon oxide or silicon nitride at temperatures typical of those used for annealing GaP (800-900°C), even though Frosch and Derick (Reference 48) show that Ga diffuses readily through thermally grown oxide layers on Si at temperatures of 1200-1300°C. Therefore, it was decided to pursue this problem employing Rutherford backscattering as the main tool; the results of the work are described in the following sections.

## 2. Ga DIFFUSION IN $\text{SiO}_x$ , $\text{SiN}_x$ , $\text{Al}_2\text{O}_3$ , AND $\text{AlN}$ - LITERATURE REVIEW

Some results have been reported in the literature that deal with the evaluation of various dielectric materials for potential use as protective coatings on semiconductors during processing. Early work by Frosch and Derick (Reference 48) on the masking properties of thermally grown  $\text{SiO}_2$  on Si, shows that Ga diffused readily through the  $\text{SiO}_2$  layer in the 1200-1300°C temperature range. Gyulai et al. (Reference 49) examined  $\text{SiO}_2$  and  $\text{Si}_3\text{N}_4$  layers on GaAs crystals that were annealed up to 800°C and show evidence for Ga out-diffusion through both types of layers. However, later work by Harris et al. (Reference 3), indicated that Ga diffuses through  $\text{SiO}_2$  but is stopped or at least strongly retarded by  $\text{Si}_3\text{N}_4$ . Because of more recent data, Mayer (Reference 50) believes that the diffusion through  $\text{Si}_3\text{N}_4$  reported in Reference 49 resulted from oxygen contamination of the films. Ga diffusion in the dielectrics  $\text{SiO}_2$ ,  $\text{Si}_3\text{N}_4$ , and  $\text{Al}_2\text{O}_3$  was examined up to anneal temperatures of 1000°C by Chu et al. (Reference 35) who ion implanted the Ga then tracked its motion with RBS (Rutherford backscattering). It is seen in Reference 35 that Ga does not move measurably in  $\text{Si}_3\text{N}_4$  or  $\text{Al}_2\text{O}_3$



after annealing for 30 minutes at 1000°C, while in SiO<sub>2</sub> it shows significant motion to the surface after 30 minutes at 800°C and after 30 minutes at 900°C most of the implanted Ga has in fact moved. The rapid Ga motion in SiO<sub>2</sub> is shown to be enhanced by the radiation damage caused to the lattice during implantation. Pashley (Reference 51, Part II, Chapters 1, 3, and 4) shows supporting evidence that Si<sub>3</sub>N<sub>4</sub> is more effective at blocking Ga motion than is SiO<sub>2</sub> and further gives evidence that AlN may be an effective coating material which possesses the additional advantage of better adherence than Si<sub>3</sub>N<sub>4</sub>, a particularly serious problem on a surface that has been implanted as shown by Eisen et al. (Reference 52) and Pashley (Reference 51, Part II, Figure 11).

It would appear in the case of GaAs, that an SiO<sub>2</sub> film not only fails to protect the surface from Ga loss, but in fact has a "leaching" effect so that coated samples which have been p-doped by implantation show an enhanced p-type behavior over non-coated samples after high temperature anneals as seen in some of Pashley's data (Reference 51, Part II, Table 1). However, the need for some sort of protective coating is necessary because Picraux (Reference 53) reports that after implantation, As is lost from uncoated GaAs samples even at the relatively low temperatures of 300°C, while Feldman et al. (Reference 4) notes that uncoated GaP decomposed to give off both Ga and P, a result supported by Sections V.4.c and V.4.d and Figures 23 and 24 of this report. It is worth noting that SiO<sub>2</sub> is apparently effective at blocking As loss as are Si<sub>3</sub>N<sub>4</sub> and Al<sub>2</sub>O<sub>3</sub> since Chu et al. (Reference 35) saw no motion during the high temperature anneals of the As which was implanted into these coatings. Presently, it can only be assumed that P is likewise blocked by SiO<sub>2</sub> and the other dielectric coatings.

3. DIFFUSION OF IMPLANTED Ga IN SPUTTERED SiO<sub>2</sub> - EXPERIMENTAL RESULTS

After trying some other approaches (Section V.4) that were not productive, it was decided to make a sandwich type sample consisting of an implanted Ga layer between two layers of SiO<sub>2</sub>. This was accomplished by sputtering an SiO<sub>2</sub> layer onto a Si substrate, ion implanting a  $4.0 \times 10^{16}/\text{cm}^2$  dose of Ga at 20keV into the central region, then overlaying with another sputtered SiO<sub>2</sub> layer that was about 1150Å thick as illustrated schematically in Figure 15. This approach which is an extension into undamaged material of the diffusion results in damaged material reported by Chu et al. in Reference 35, was suggested by Davies (Reference 54) after the problems described in Section V.4.b of this report arose with the evaporated layers. The sandwich was examined before and after a series of anneals in flowing argon at 850°C. This structure allows "tracking" of the Ga with RBS as long as it remains in the SiO<sub>2</sub> and permits observing the changing profile of the main Ga peak or source. This approach also eliminates any other Ga sources which are present when looking at SiO<sub>2</sub> on GaP, an approach mentioned below that was tried and abandoned because of the contamination problem.

Figure 16 shows the RBS spectrum of the first SiO<sub>2</sub> layer on the Si substrate with the probe beam at an angle of 10° to the sample surface ( $\theta_1 = 80^\circ$ ). The Si edge is located as it should be at channel 226.7 for 2 MeV  $\alpha$ -particles and the multichannel analyzer setting of 5keV/channel. The method illustrated in Section IV.1 can be employed here to measure the film thickness by observing from Figure 16 how far the Si substrate edge has been shifted from the surface Si position of channel 226.7 which is now occupied by Si at the surface of the SiO<sub>2</sub>. The new Si substrate edge position (in Figure 9 for  $\theta_1 = 80^\circ$  and  $\theta_2 = -68^\circ$ ) is at



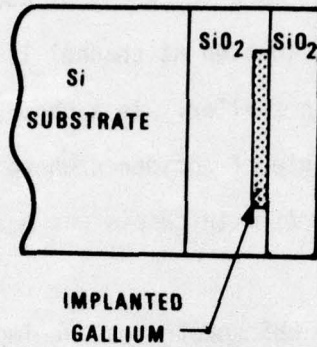


Figure 15. Schematic Illustration of the Sandwich Structure Employed for Studying the Diffusion of Ga in SiO<sub>2</sub>.

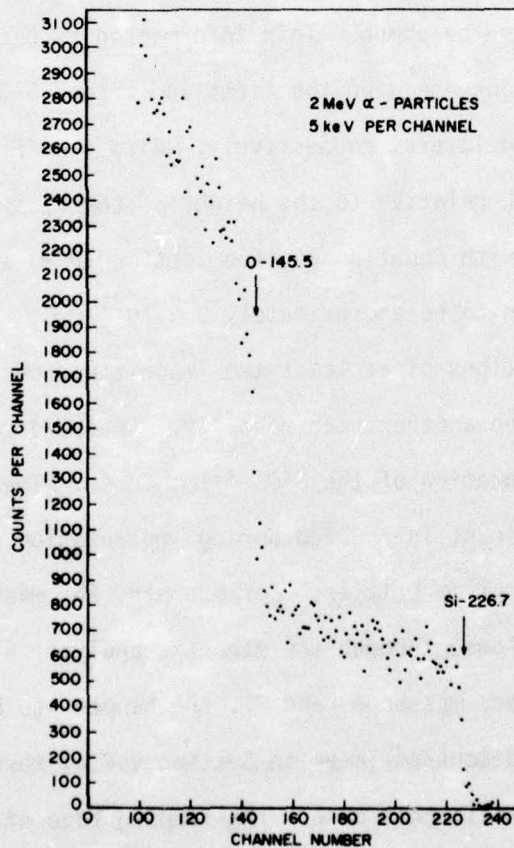


Figure 16. RBS Spectrum of SiO<sub>2</sub> on Si. The Film Thickness is About 2610Å, Calculated Using the Shift in the Substrate Si Edge from the Surface Position (Channel No. 226.7) to Channel No. 144.5.

channel 144.5 which leads to a thickness of about  $2610\text{\AA}$ . It should be noted that the 0 edge is located at channel 145.5 and thus overlaps the Si substrate edge, but is smaller. As a check, the  $\text{SiO}_2$  thickness was determined at another angle of incidence where the edges did not interfere and nearly the same film thickness was measured.

Figure 17 shows the RBS spectrum after implanting the  $4.0 \times 10^{16}/\text{cm}^2$  dose of Ga into the sample of Figure 16. The primary value of this Figure 17 is to establish the position of the Ga relative to the  $\text{SiO}_2$  surface by noting that Ga on the surface should appear at channel 318.6 which is indicated on the graph. This information is used in Figure 18 to identify the boundary between the first and second  $\text{SiO}_2$  layers or the damaged and undamaged layers, respectively. Also from Figure 18 the height of the Ga peak relative to the height of the Si spectrum near channel 220 is used with Equation 24 (see Section IV.1) to estimate the Ga peak concentration to be approximately  $9 \times 10^{21}/\text{cm}^3$ . Also visible in Figure 17 are indications of at least two impurities, one near the mass of Ar as indicated and another near mass 159. Ar could easily be present due to the preparation of the  $\text{SiO}_2$  films in Ar. The heavy mass is most likely a contaminant introduced during implantation due to double or triple ionization of impurities. For example, Pb, mass 207.2 when triply ionized is allowed through the magnetic analyzer along with the singly ionized Ga ions, masses 69 and 71. Pb happens to be a common problem, as will be discussed later in Section V.4.a, therefore, is most likely the contaminant in this case. The leading edge of the impurity peak in Figure 17 does not coincide with the indicated position of surface Pb at channel 370.5 because it was implanted with an energy of



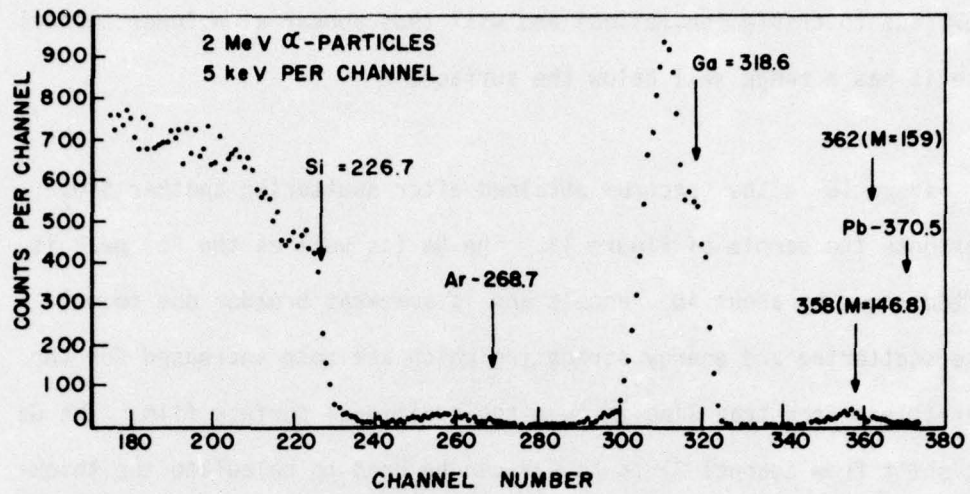


Figure 17. RBS Spectrum of the Sample in Figure 16 after Implantation of Ga to a Dose of  $4.0 \times 10^{16}/\text{cm}^2$ . The Ga Edge is Calculated to Appear at Channel No. 318.6.

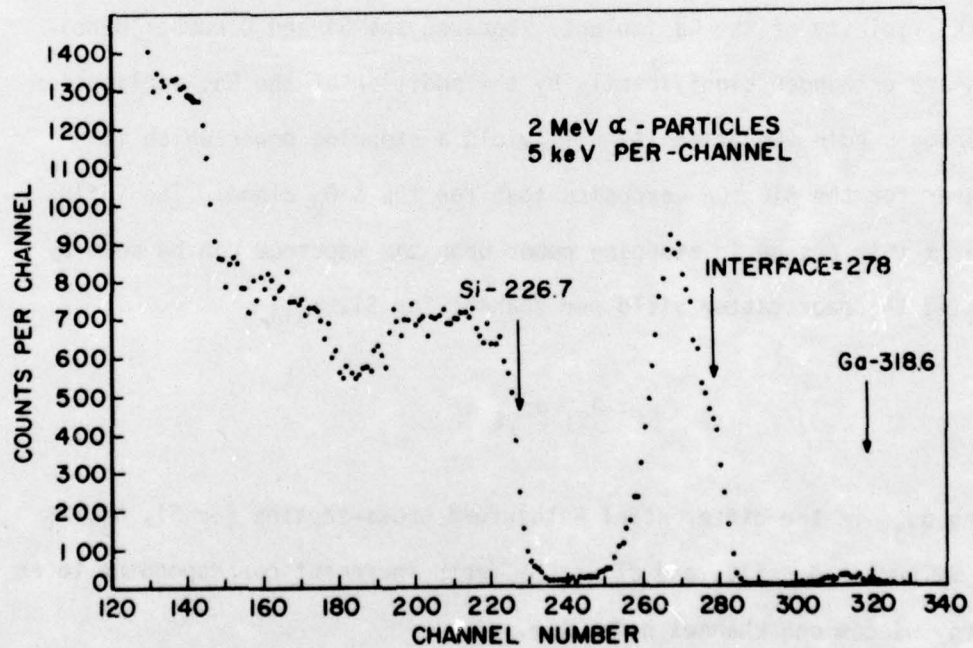


Figure 18. RBS Spectrum of the Sample in Figure 17 After the Addition of a  $\text{SiO}_2$  Film. The Interface Between the First (Figure 16) and Second Films is Found to be at Channel No. 278 by Comparison to Figure 17.

60keV (due to triple ionization) and will thus appear at a lower channel since it has a range well below the surface.

Figure 18 is the spectrum obtained after sputtering another  $\text{SiO}_2$  layer onto the sample of Figure 17. The Ga (as well as the Pb) peak is shifted lower by about 40 channels and is somewhat broader due to multiple scattering and energy straggling which are both increased for the  $\alpha$ -particles after traveling through the additional surface film. The Ga peak shift from channel 318.6 to 278 can be used to calculate the thickness of the new surface film which is found to be about 1130 $\text{\AA}$ . It is interesting to note that a dip in the Si spectrum of Figure 18 is seen centered near channel 185 which corresponds to the location of the Ga in the  $\text{SiO}_2$ . The dip results from the increased stopping power of the  $\text{SiO}_2$  in the vicinity of the Ga implant. Because the Si and O number densities are unchanged significantly by the addition of the Ga, application of Bragg's rule (Equation 14) will yield a stopping power which is greater for the  $\text{SiO}_2$ :Ga composite than for the  $\text{SiO}_2$  alone. The influence of this change in stopping power upon the spectrum can be seen by writing the backscatter yield per channel for Si,  $Y_{\text{Si}}$ ,

$$Y_{\text{Si}} \propto N_{\text{Si}} d\sigma_{\text{Si}} dZ$$

where  $d\sigma_{\text{Si}}$  is the differential Rutherford cross-section for Si,  $N_{\text{Si}}$  is the Si number density, and  $dZ$  is the depth increment corresponding to an energy window one channel wide, i.e.

$$dZ = \frac{\Delta E}{[S]}$$



where  $\Delta E$  is the energy per channel and  $[S]$  is the stopping power function defined by Equation 28. Therefore,

$$Y_{Si} \propto \frac{N_{Si} d\sigma_{Si} \Delta E}{[S]}$$

which clearly shows how an increase in  $[S]$  results in a decreased backscatter yield for Si in the vicinity of any impurities that may be present. The same sort of dip would be present in the 0 portion of the spectrum but is not visible due to a low signal/noise ratio. This dip in the Si spectrum of Figure 18 is not seen in "ordinary" RBS spectra run at normal incidence ( $\theta_1 = 0$ ) but becomes visible at  $\theta_1 = 80^\circ$  due to the increased resolution of the glancing incidence technique as described by Williams (References 14, 15).

Figure 19 shows the sample of Figure 18 after a 30-minute anneal at  $850^\circ\text{C}$  in flowing Ar. The main points of interest are the shift of the main or "source" Ga peak up to the interface, the formation of a small Ga peak on the sample surface, the appearance of some Ga between the source and surface peaks, and the reduction in the total amount of Ga detected by about 20%. Note that the motion of the source peak quickly through the damaged material up to the interface with the undamaged  $\text{SiO}_2$  film is consistent with the results reported by Chu et al. (Reference 35).

A RBS spectrum of this sample was also run at normal incidence to check for diffusion toward the Si substrate; the results showed diffusion toward the surface only and were consistent with Figure 19.

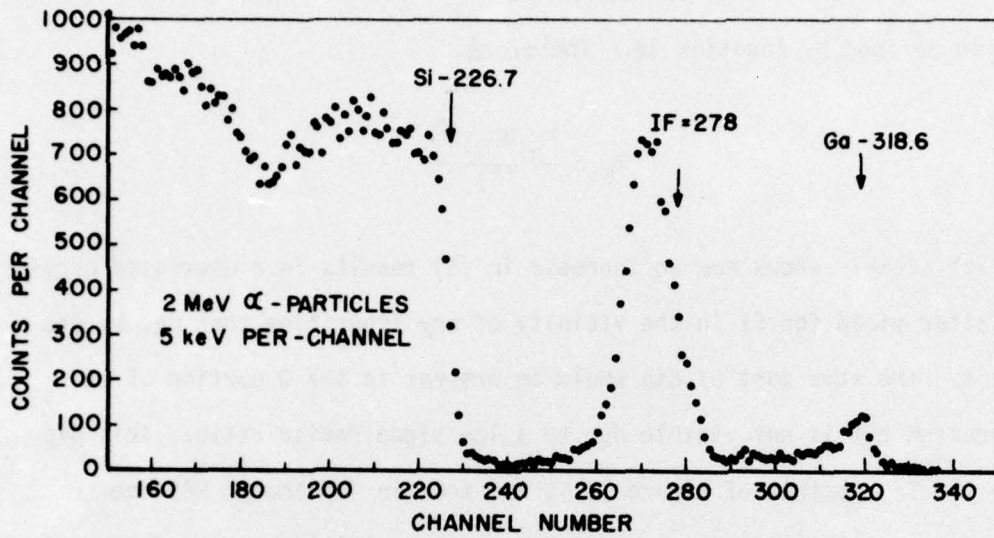


Figure 19. RBS Spectrum of the Sample in Figure 18 After a 30-Minute Anneal at 850°C. Note, the Shift in the Main Ga Peak to the Interface (IF) and the Appearance of a Ga Peak at the Surface.

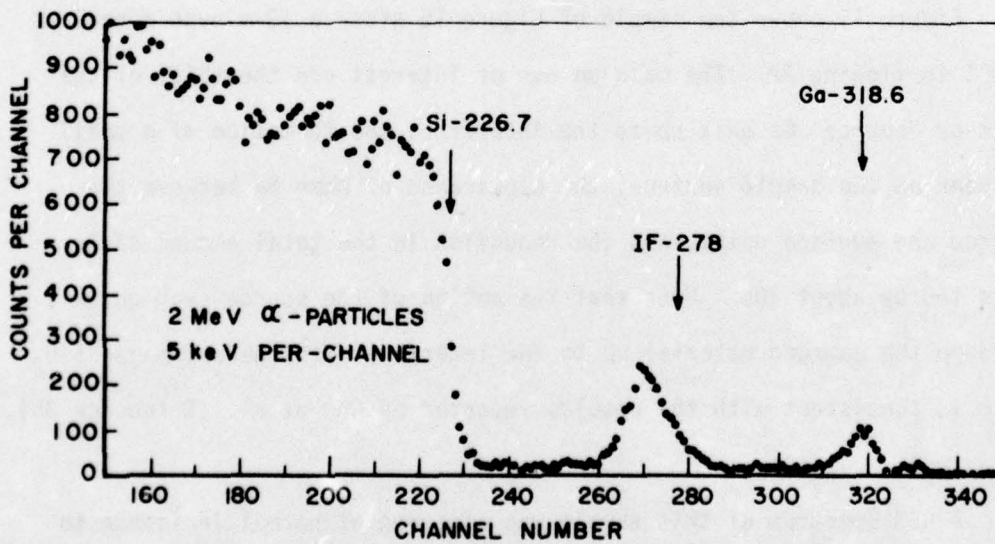


Figure 20. RBS Spectrum of the Sample in Figure 18 After a 4 1/2 Hour Anneal at 850°C.



Four more 30-minute anneals and then a 2-hour anneal were performed, resulting in a series of anneals at 1/2, 1, 1-1/2, 2, 2-1/2, and 4-1/2 hours. After each anneal, RBS spectra were taken at 10° and 90° incidence, and in some cases at more than one spot to check consistency over the surface, which was quite good. The data from the spectra taken at 10° incidence were plotted and the relative amounts of Ga present were measured by taking the Total Integrated Count or TIC under the source and surface peaks, that is, by adding the counts in each channel from channel 245 through channel 330. Care was taken in each run to expose the sample to the same integrated beam current, thus all the spectra result from equal numbers of particles striking the target during the collection of the data. In this way the TIC for the Ga of each run can be compared to the other runs and will represent the relative amount of Ga present. An estimate of the absolute amount of Ga can be obtained as shown previously in Section IV.1 by comparing the Ga peak to the Si spectra in which the Si concentration is known.

In Figure 20 is plotted the spectrum of Figure 18 after a 4 1/2-hour anneal. The main features of note in Figure 20 are the position of the source peak which has stayed against the interface with the undamaged SiO<sub>2</sub>, the size of the source peak which has decreased dramatically from its size before annealing (Figure 18), the width at half-height of the source peak which has remained essentially unchanged, the size of the surface Ga peak which has remained nearly constant, and the disappearance of the dip near channel 185 in the Si spectrum.

Again, it is worth noting that checks at 90° incidence after the various anneals showed no indication of Ga motion toward the Si substrate.

The major property of the spectra that has changed through the series of anneals is the TIC of Ga which is plotted in Figure 21 as a function of anneal time. Table 1 lists the total TIC data for the various anneals as well as the surface peak and source peak TIC's.

TABLE 1 - TIC VALUES

Anneal Time (hours)	Total TIC (counts)	Source Peak TIC	Surface Peak TIC
0	15,328	15,328	0
1/2	12,381	10,859	1,522
1	10,018	8,877	1,141
1-1/2	10,087	8,910	1,177
2	8,374	6,957	1,417
2-1/2	5,749	4,713	1,036
2-1/2	6,544	5,528	1,016
4-1/2	4,600	3,449	1,151

After 4 1/2 hours of annealing, the source peak is only a little over three times as large as the surface peak, but the surface peak remains nominally constant through the whole process. This observation would seem to indicate that the surface peak size is controlled by the temperature and the material ( $\text{SiO}_2$ ) such that the Ga evaporates only while new Ga is supplied but will not drop below a concentration (approximately  $5.9 \times 10^{20}/\text{cm}^3$ ) which yields the observed TIC of about 1100 counts even though the source may be depleted.



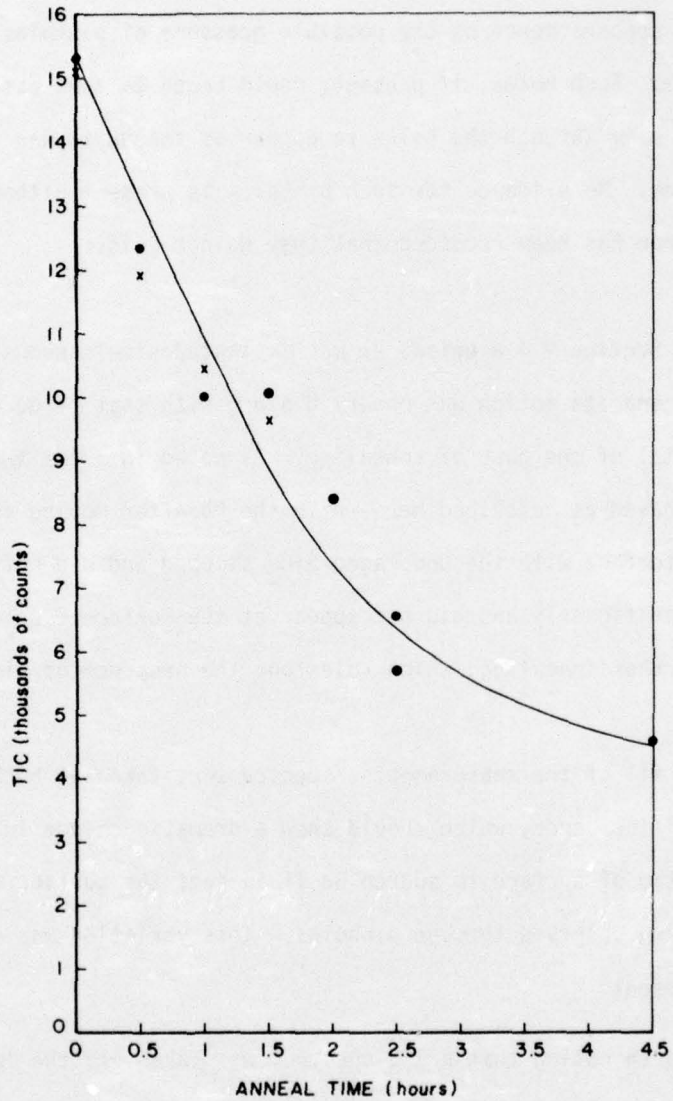


Figure 21. Relative Amounts of Ga Observed in the RBS Spectra Before Annealing and After Each Anneal at 850°C up to 4 1/2 Hours. The TIC (Total Integrated Count) Is Proportional to the Total Amount of Ga Present. The (.) Symbols Are for the Data of this Section (Table 1) and the (X) Symbols for the Data of Section V.4.b (Table 2).

A question that may arise concerning the explanation presented for the observed spectra concerns the possible presence of pinholes in the top  $\text{SiO}_2$  film. Such holes, if present, could cause Ga that was observed by the probe beam through the holes to appear as though it was located on the surface. No evidence for such pinholes is present although strong evidence has been recorded that they do not exist:

- 1) in Section V.4.a below, Pb was implanted simultaneously with Ga and its motion was observed along with that of Ga during a total of one hour of annealing. As noted in V.4.a the Ga behaved as described here while the Pb after moving to the interface with the undamaged  $\text{SiO}_2$  stopped and did not decrease significantly and did not appear at the surface even after further annealing, which rules out the presence of pinholes,
- 2) in all of the measurements, spectra were taken at both  $10^\circ$  and  $90^\circ$  incidence, which should show a dramatic change in the ratio of surface to source Ga if in fact the surface peak was being observed through pinholes. This variation was not present.

It is worth noting that a RBS spectrum was taken off the implant region of the sample, but near to the implant where the  $\text{SiO}_2$  had become somewhat discolored during the annealing. The only trace of Ga in the spectrum was a very small surface peak with no evidence of in-diffusion. It would seem feasible that this peak is the result of condensation of Ga that has been evaporated from the surface peak of the implanted region.



The experimental results of Ga diffusion in  $\text{SiO}_2$  are summarized below:

- 1) the source peak width at half-height remains nearly constant,
- 2) no motion by Ga toward the substrate is observed,
- 3) the surface peak forms during the first 1/2-hour anneal and remains essentially constant through 4 1/2 hours of annealing while the source peak decreases by over a factor of four,
- 4) a check outside the implanted region, but near to it, shows a small surface Ga peak which may arise from evaporation from the implanted region or from surface diffusion,
- 5) the source peak moves quickly as a whole up to the interface between the implanted and unimplanted (damaged and undamaged)  $\text{SiO}_2$  layers, with nearly all the motion occurring during the first 1/2-hour anneal,
- 6) the source peak Ga appears to "leak" into the undamaged or top  $\text{SiO}_2$  film, but once across the interface it moves rapidly to the surface because very little Ga is seen between the interface and the surface peak, though more is observed after the start of annealing than before. The surface peak does not

grow (or shrink) beyond a reasonably well fixed size in spite of the fact that it is being continually "fed" at the changing rate by the source peak that decreases in size by over a factor of four, which strongly supports the assumption that Ga is evaporating from the surface at a rate determined by the rate at which it is supplied with Ga,

- 7) the rate of decrease in the source peak flattens out at long anneals due to the fact that it is being depleted, and
- 8) it is not possible, due to the nature of RBS (see the introduction), to comment as to whether or not the Ga is combined with the O in some way and if so, how.

#### 4. Ga DIFFUSION IN $\text{SiO}_2$ - OTHER EXPERIMENTAL APPROACHES

Before settling on the sandwich technique described in Section V.3, some other approaches were explored for evaluating the motion of Ga in  $\text{SiO}_2$ . Each of these experiments proved unsatisfactory for some reason in terms of not addressing the main question or by introducing some factor that made the results questionable. Each did, however, prove instructive in terms of using the RBS method for thin film analysis.

##### a. Simultaneous Implantation of Pb and Ga into $\text{SiO}_2$

The first  $\text{SiO}_2:\text{Ga}:\text{SiO}_2$  implantation sandwich was prepared (Figure 15) with Pb also present in the source region of the separator. Since triply ionized Pb (mass = 207) will pass through the magnetic



analyzer with Ga, it was simultaneously implanted. The peak concentration of Pb measured from the RBS data was approximately 10% of the Ga peak concentration which was about  $1.6 \times 10^{21}$  Ga ions/cm<sup>3</sup>. The backscatter spectrum of the sandwich before annealing is shown in Figure 22.

This sample was given two 1/2-hour anneals at 850°C for a total of one hour. After each anneal a RBS spectrum was taken at 10° and 90° so the motion of both the Ga and Pb could be observed:

- 1) the Pb moved to the interface with the undamaged SiO<sub>2</sub> during the first anneal, then remained stationary; it did not show any measurable diffusion to the surface or decrease in size during the second anneal,
- 2) most of the Ga moved quickly to the interface during the first anneal and some diffused to the surface, consistent with Section V.3 above,
- 3) on the second anneal, the source peak decreased in size quite dramatically while the surface peak remained about constant, also consistent with Section V.3, and
- 4) the major deviation from Section V.3 was the observation that a small part of the "Ga" peak seemed to remain behind and showed no motion during either anneal. It seems likely that this may be an impurity introduced during the sample preparation, though not necessarily during implantation since it could be another mass and/or at a different depth than the Ga.

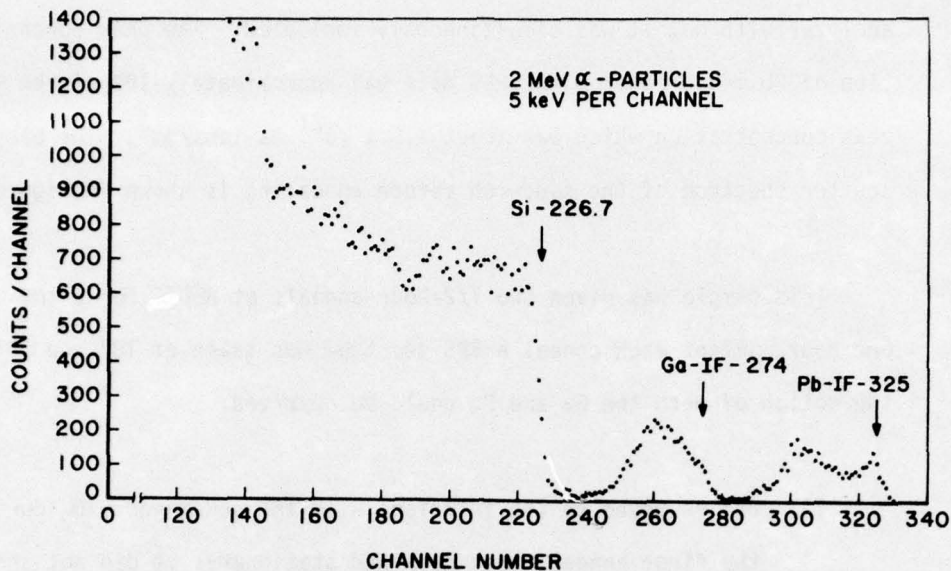


Figure 22. RBS Spectrum of a Ga - Pb Implant into a  $\text{SiO}_2$  Film on Si, Over-coated with  $\text{SiO}_2$ .

To establish more information about the unknown peak described in 4) above, the RBS spectra taken at  $90^\circ$  incidence were examined and showed another small peak located at a lower energy than the Ga peak, even before annealing, and its position and size were constant through the two anneals. Its depth was determined to be in the vicinity of the interface between the two  $\text{SiO}_2$  layers because in going from  $\theta_1 = 80^\circ$  to  $\theta_1 = 0^\circ$ , its position shifted by nearly the same number of channels as did the Ga and Pb peaks. It was estimated from this information, that if the unknown peak were located at the surface, it would fall at channel 300 which permitted a mass estimate of  $M = 55$  to be calculated.

Because of the presence of impurities other than Ga, this sample was not accepted for use in supplying the main data on the diffusion behavior of Ga in  $\text{SiO}_2$ .



b. Evaporation of Ga onto SiO<sub>2</sub>

The initial attempt at making a SiO<sub>2</sub>:Ga:SiO<sub>2</sub> sandwich structure involved depositing a Ga layer on the oxide layer, then overcoating with another oxide film. After preparation and before annealing, however, it became apparent that the top SiO<sub>2</sub> layer had mixed with the Ga film, rather than coating over the top of the Ga. This was concluded from the RBS spectrum since the Ga peak has a smooth Gaussian-like shape for the 200Å (and 600Å) thick film rather than a flat-top profile as it would have for a continuous pure Ga layer. Further, the dip in the Si profile (Figure 18) in the vicinity of the Ga did not drop to zero as it would for a pure continuous Ga film of that thickness. In fact, the RBS spectra looked very much like Figure 18 in which the Ga had been implanted. Also, the mixing proposal is consistent with the thickness of the top SiO<sub>2</sub> film measured from the shift in the Ga edge, which was much less than would be the case if the SiO<sub>2</sub> were totally on top of a continuous film.

In spite of this behavior, three anneals were run at 850°C for 1/2, 1, and 1 1/2 hours. The results turned out to be very similar to those described in Section V.3 for the implanted sandwich. In particular, the Ga TIC (Total Integrated Count) for the deposited 200Å film follows very closely the data of Figure 21 for the same anneal times (see the Xs in Figure 21) after the normalization to compensate for different running times during RBS data collection. The collected TIC data is shown in Table 2.

TABLE 2. TIC VALUES

Anneal Time (hours)	Total TIC (counts)	Source Peak TIC	Surface Peak TIC
0	15,126	15,126	0
1/2	11,925	11,400	525
1	10,440	9,801	639
1-1/2	9,630	9,069	561

Overall, the general diffusion behavior in this sample appeared quite similar to the implanted sandwich described in Section V.3:

- 1) a surface peak formed during the first 1/2-hour anneal and remained essentially constant, though smaller than the implanted sample,
- 2) the Ga seemed to move only to the surface, not back towards the substrate,
- 3) the Ga peak showed no significant broadening during annealing, and
- 4) the Ga peak did not move as a whole which the implanted peak did in its motion up through the damaged material to the interface.

c.  $\text{SiO}_2$  Coating on Implanted GaP

A direct approach to evaluating  $\text{SiO}_2$  as a protective coating on implanted GaP was taken by implanting a specimen with 40keV Zn ions to a



AFML-TR-75-55

dose of  $10^{16}$  ions/cm<sup>2</sup> then coating both sides with sputtered SiO<sub>2</sub> to a thickness of about 1300Å. The sample was examined by RBS before annealing, then after total anneals of 5, 25, and 85 min., at 850°C. Because of the similarity in mass between Zn and Ga, Zn was not resolvable as expected. The first Ga visible outside the substrate in the RBS spectra appeared on the front (implanted) side as a very small peak at the surface of the SiO<sub>2</sub> after 25 minutes at 850°C. After an additional 60 minutes (85 minutes total) at 850°C, a large Ga peak was present on the front surface as well as a P peak which is seen superimposed on the substrate spectrum in Figure 23.

Figure 23 indicates that a GaP film has formed on the surface of the SiO<sub>2</sub> which implies that GaP has evaporated through a hole or defect in the SiO<sub>2</sub> and then condensed on the surface. Unfortunately, no strong evidence is present to indicate Ga diffusion through the film since no Ga is detectable in the SiO<sub>2</sub> film on either the front or back of the sample. To pursue this approach further, both sides of the sample were coated again with SiO<sub>2</sub> and annealed for total times of 15, 30, and 90 minutes. Again, a surface peak formed on the front which became quite large in 90 minutes as shown in Figure 24. In addition to the Ga peak, Figure 24 shows, like Figure 23, a P peak at the surface which again points to evaporation and recondensation of GaP on top of the SiO<sub>2</sub> film. Spectra taken of the back (unimplanted side) showed only a rather small surface Ga peak, which was however, considerably larger after the second series of anneals than after the first set.

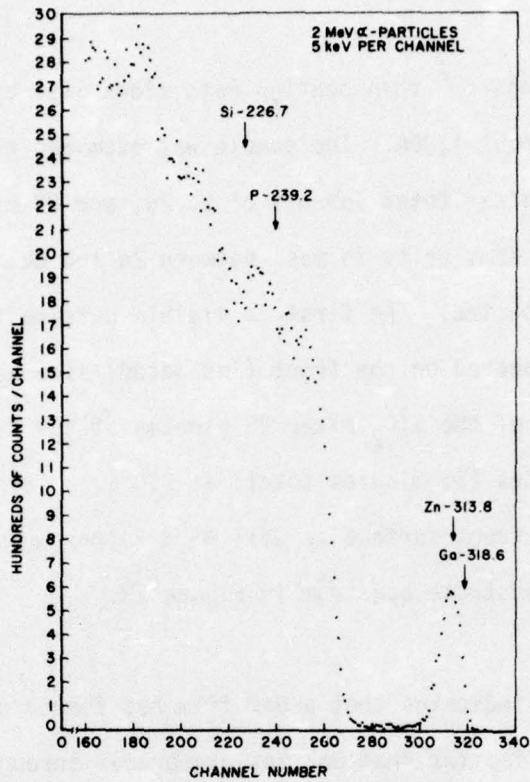


Figure 23. RBS Spectrum of a GaP Crystal Implanted with Zn to a Dose of  $10^{16}/\text{cm}^2$ , Coated with  $\text{SiO}_2$ , and Annealed for 85 Minutes at  $850^\circ\text{C}$ . Note that Ga and P Are at the Surface But Si is Shifted Back, Indicating a GaP Surface Film.

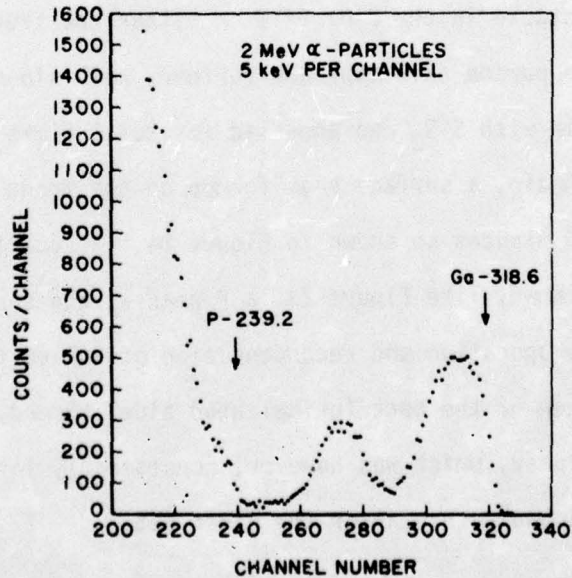


Figure 24. RBS Spectrum of the Sample of Figure 23 Coated Again with  $\text{SiO}_2$  and Annealed for an Additional 90 Minutes at  $850^\circ\text{C}$ . Again, Note the Presence of Ga and P at the Surface Indicating a New GaP Surface Film.



The results of this series permitted no definite conclusions to be drawn concerning the diffusion of Ga in SiO<sub>2</sub> as is apparent in the following summary:

- 1) GaP appears to be evaporating through a hole in the SiO<sub>2</sub> film and recondensing on the surface,
- 2) the SiO<sub>2</sub> film on the implanted side showed a bubbly appearance after the first few anneals under a low power microscope (about 30X), especially in those regions that had been probed for the RBS data,
- 3) some Ga is apparently moving through the SiO<sub>2</sub> because after the second SiO<sub>2</sub> layer was added, the internal Ga peak shrunk during the annealing but could not be definitively tracked due to the growth of the Ga peak on the surface, Figure 24, and
- 4) the presence of Ga could not be positively detected within the SiO<sub>2</sub> film on either side of the sample.

d. SiO<sub>2</sub> Coating on GaP Examined by Channeling

In another attempt to sensitively measure surface motion of Ga from GaP into SiO<sub>2</sub>, a single crystal specimen was coated with a thin (250-300Å) layer of sputtered SiO<sub>2</sub>. The sample was then examined before and after annealing for 1/2 hour at 850°C by making random and channeled RBS spectra in an effort to observe changes in the Ga/P ratio of the surface

peaks. This approach was suggested by J. A. Davies (Reference 54) and was directed along the same lines as the surface studies described by Morgan and Bøgh (Reference 21) and by Morgan and Wood (Reference 22) in which several preparation techniques of single crystals were compared and evaluated using channeling and comparison of the surface peaks.

Unfortunately, after annealing, a large GaP film appeared on top of the  $\text{SiO}_2$  which masked any changes in the surface peaks that may have occurred. Presumably, the GaP came from the substrate since only the front was coated, a result consistent with the observations made by Feldman et al. (Reference 4). Even though coating the back of the sample and using a shorter anneal may have yielded useful results, this approach was pursued no further primarily because the  $\text{SiO}_2$  film was so thin that it would have been very difficult if not impossible to locate any Ga that did in fact leave the surface.

The observed results did have the positive impact of supporting the caution taken when examining the annealed GaP specimens that had been coated on both sides (Section V.4.c). In that former case it was assumed that GaP may have escaped through cracks and holes in the film after anneals of over one hour at  $850^\circ\text{C}$ . In this case, after observing a large GaP layer on the  $\text{SiO}_2$  after only a 1/2-hour anneal, it appears even more feasible that the assumption made in Section V.4.c was correct.



## SECTION VI

## SUMMARY AND SUGGESTED FUTURE WORK

## 1. SUMMARY

The initial goal of examining the motion of the Ga in silicon dioxide films has been accomplished using the Rutherford backscattering technique. With this method, it has been possible during a series of anneals to track and record the motion of Ga in undamaged material, and to some extent in damaged material where it appeared to move more easily. Simultaneously Pb was observed to move in damaged  $\text{SiO}_2$ , but remain stationary at the interface with the undamaged film.

These results not only furnish data for the selection or rejection of  $\text{SiO}_2$  as a protective coating material, but also outline a method by which other potential candidate films (e.g.  $\text{AlN}$ ,  $\text{Si}_3\text{N}_4$  and  $\text{Al}_2\text{O}_3$ ) can be evaluated. Additionally, the application of the RBS technique to the measurement of other critical materials properties such as stoichiometry, thickness, and impurity content and location is discussed and demonstrated.

## 2. SUGGESTED FUTURE WORK

The RBS method described here can be applied to other problems, some of which would further clarify the role of protective layers on GaP, and others that would be an extension of the technique:

- 1) examination of the diffusion characteristics of P in  $\text{SiO}_2$  and perhaps other films such as  $\text{Si}_3\text{N}_4$  using the sandwich technique,

- 2) checking the diffusion of Ga in a  $\text{Si}_3\text{N}_4$  sandwich,
- 3) evaluating protective films on GaP directly by evaporating a GaP film onto a C substrate, coating with  $\text{SiO}_2$ , then tracking any Ga or P motion during anneals (suggested by Williams (Reference 55)),
- 4) tracking diffusion in AlN by the sandwich method,
- 5) checking to see if the Ga surface peak after annealing (Section V.3) takes on different sizes at different anneal temperatures, and
- 6) making a more careful attempt to see Ga loss from the surface of a single crystal using the method of Section V.4.d by coating both sides of the sample, using shorter anneals, and obtaining better statistics.

RBS, as demonstrated, has and can supply information about the motion of Ga in passivating films, however, more work is required to evaluate the role of the films when they are actually on the semiconductors. For example, the approach employed by Hemenger and Dobbs (Reference 29) and discussed in Section V.1 using electrical measurements could be expanded to compare the growth of p-type conductivity during annealing in both implanted and unimplanted crystals which are coated with  $\text{SiO}_2$ . Also, the SEM (scanning electron microscope) could be used to directly track p-layer growth (Section V.1) and to observe the physical quality of the passivating films on implanted and unimplanted material (e.g. see Pashley, Reference 51, Part II, Figure 11).



APPENDIX - TABLE OF  $k^2$  AND CROSS-SECTION VALUES

Following is a table containing two types of calculated numbers that were used repeatedly during analysis of the RBS spectra. First are  $k^2$  values calculated for a variety of target masses using Equation 4. In the next column are shown cross-section values calculated using Equation 21 but with all terms removed that cancel when forming a ratio of cross-sections (Equation 24). Both columns were calculated using  $M_1 = M_{\text{He}} = 4.0026$  and  $\phi = 168^\circ$  which are the values used for all of the spectra in this report.

AD-A031 740

AIR FORCE MATERIALS LAB WRIGHT-PATTERSON AFB OHIO  
GALLIUM DIFFUSION IN SILICON DIOXIDE. RUTHERFORD BACKSCATTERING--ETC(U)  
MAY 76 P M HEMENGER  
AFML-TR-75-55

F/G 7/2

UNCLASSIFIED

NL

2 of 2  
AD  
A031740



END

DATE  
FILMED  
12-76



AFML-TR-75-55

Element	Mass	$Z_2$	$k^2$	$\phi = 168^\circ$	$\beta = M_{\text{He}}/M_2$
				$(2E/Z_1 e^2)^2 (d\sigma/d\Omega)_{\text{lab.}} \sin^4 \phi$	
C	12.01115		0.253778		
N	14.0067	7	0.312458		0.0198036
O	15.9994	8	0.363694		0.0269292
F	18.9984	9	0.428989		0.0353905
Al	26.9815	13	0.553601		0.0772632
Si	28.086	14	0.566813		0.0899115
P	30.9738	15	0.598003		0.1039606
S	32.064		0.608665		
Ar	39.948		0.671829		
Ca	40.08		0.6727		
Cu	63.54	29	0.779148		0.3984883
Zn	65.37	30	0.784624		0.42662764
Ga	69.72	31	0.796616		0.4559491
"	69		0.794724		
"	71		0.799896		
As	74.922		0.809318		
Se	78.96	34	0.818138		0.5492496
Ag	107.87		0.863407		
Cd	112.40	48	0.868537		1.0974949
Cs	132.905		0.887643		
Hf	178.49	72	0.915089		2.4730668
W	183.85		0.91746		
Au	196.967	79	0.92274		2.97784
Pb	207.19	82	0.926409		3.2085498
Bi	208.98		0.927016		
Cl	35.453	17	0.638525		0.1345843
K	39.102	19	0.666032		0.16887059

## REFERENCES

1. J. W. Mayer, L. Eriksson, and J. A. Davies, Ion Implantation in Semiconductors, Academic Press, New York (1970).
2. J. W. Mayer, *Rad. Effects* 12, 183-191 (1972) "Semiconductor Physics and Channeling".
3. J. S. Harris, F. H. Eisen, B. Welch, J. D. Haskell, R. D. Pashley, and J. W. Mayer, *Appl. Phys. Letters* 21, 601-603 (1972) "Influence of Implantation Temperature and Surface Protection on Tellurium Implantations in GaAs".
4. L. C. Feldman, W. M. Augustyniak, and J. L. Merz, *Rad. Effects* 6, 293-299 (1970) "Implantation of Bi Into GaP".
5. Channeling, ed. by D. V. Morgan, John Wiley and Sons, New York (1973).
6. S. T. Picraux, California Institute of Technology. Scientific Report #1, April 1969 under Contract F19628-68-C-0142, Report #AFCRL-69-0199. AD 689 187. "Channeling in Semiconductors and its Application to the Study of Ion Implantation".
7. G. Carter and J. S. Colligon, Ion Bombardment of Solids, American Elsevier Pub. Co., Inc., New York (1968).
8. R. B. Leighton, Principles of Modern Physics, McGraw-Hill, New York (1959), p. 485.
9. D. G. Armour and G. Carter, *J. Phys. E: Sci. Instr.* 5, 2-8 (1972) "Analysis of Backscattered Ions as a Technique for the Study of Surfaces".
10. E. Bøgh, *Rad. Effects* 12, 13-19 (1972) "An Application of High Energy-Resolution Scattering Measurements in Channeling Studies".
11. I. Bergström, K. Björkqvist, B. Domeij, G. Fladda, and S. Anderson, *Can. J. Phys.* 46, 2679-2682 (1968) "Critical Angles for Channeling of Low Energy Ions in Tungsten".
12. W. K. Chu, J. W. Mayer, M. -A. Nicolet, T. M. Buck, G. Amsel, F. Eisen, *Thin Solid Films* 17, 1-41 (1973) "Principles and Applications of Ion Beam Techniques for the Analysis of Solids and Thin Films".
13. L. C. Northcliffe and R. F. Schilling, *Nuclear Data Tables* A7, 233-463 (1970) "Range and Stopping-Power Tables for Heavy Ions".
14. J. S. Williams, *Nucl. Instrum. and Meth.*, 126, 205-215 (1975) "The Optimization of a Rutherford Backscattering Geometry for Enhanced Depth Resolution".
15. J. S. Williams, *Rad Effects* 22, 211-213 (1974) "Range and Stopping Power Effects Obtained from High Resolution Rutherford Backscattering Analysis of Implanted Targets".



16. W. K. Chu, B. L. Crowder, J. W. Mayer, and J. F. Ziegler, *Appl. Phys. Letters* 22, 490-492 (1973) "Range Distribution of Implanted Ions in  $\text{SiO}_2$ ,  $\text{Si}_3\text{N}_4$ , and  $\text{Al}_2\text{O}_3$ ".
17. D. A. Thompson and W. D. Mackintosh, *J. Appl. Phys.* 42, 3969-3976 (1971) "Stopping Cross Sections for 0.3-1.7 MeV Helium Ions in Silicon and Silicon Dioxide".
18. J. S.-Y. Feng, W. K. Chu, and M. -A. Nicolet, *Thin Solid Films* 19, 227-238 (1973) "Bragg's Rule Study in Binary Metal Alloys and Metal Oxides for MeV  $^4\text{He}^+$  Ions".
19. J. F. Ziegler and J. E. E. Baglin, *J. Appl. Phys.* 42, 2031-2040 (1971) "Determination of Surface Impurity Concentration Profiles by Nuclear Backscattering".
20. J. O. Hvalgård, S. L. Anderson, and T. Olsen, *Phys. Stat. Sol. (a)* 5, K83-K86 (1971) "Surface Preparation of Single Crystal n-Type GaAs Substrates Studied by the Channeling Technique".
21. D. V. Morgan and E. Bøgh, *Surface Science* 32, 278-286 (1972) "On the Application of Rutherford Scattering and Channeling Techniques to Study Semiconductor Surfaces".
22. D. V. Morgan and D. R. Wood, *Proc. Roy. Soc. Lond. A.* 335, 509-523 (1973) "Surface Studies by Means of  $\alpha$ -Particles of High Energy (2-4MeV)".
23. G. Carter and J. L. Whitton, *Rad. Effects.* 15, 143-148 (1972) "Ion Implantation Damage and Annealing in GaP".
24. O. Meyer, J. Gyulai, and J. W. Mayer, *Surface Science* 22, 263-276 (1970) "Analysis of Amorphous Layers on Silicon by Backscattering and Channeling Effect Measurements".
25. R. S. Blewer, *Appl. Phys. Letters* 23, 593-595 (1973) "Depth Distribution of Implanted Helium and Other Low-Z Elements in Metal Films Using Proton Backscattering".
26. D. Vernon Morgan, *J. Phys. D: Appl. Phys.* 7, 653-662 (1974) "Thin Film Analysis Using Rutherford Scattering".
27. J. W. Mayer and A. Tuross, *Thin Solid Films* 19, 1-10 (1973) "Comparison of Surface Layer Analysis Techniques".
28. J. W. Mayer, I. V. Mitchell, and M. -A. Nicolet, *Ion Implantation in Semiconductors*, ed. by I. Ruge and J. Graul, Springer-Verlag, N.Y. (1971) pp. 274-286 "Analysis of Contact Formation and Surface Layers on Semiconductors".
29. P. M. Hemenger and B. C. Dobbs, *Appl. Phys. Letters* 23, 462-464 (1973) "Zinc Ion Implantation of Sulfur-Doped GaP".
30. G. Dearnaley, A. M. Stoneham, and D. V. Morgan, *Rep. Prog. Phys.* 33, 1129-1191 (1971) "Electrical Phenomena in Amorphous Oxide Films".

31. D. V. Morgan and R. P. Gittens, Phys. Stat. Sol. (a) 13, 517-526 (1972) "An Investigation of the Stoichiometry and Impurity Content of Thin Silicon Oxide Films Using Rutherford Scattering of MeV  $\alpha$ -Particles".
32. W. K. Chu, E. Lugujo, J. W. Mayer, and T. W. Sigmon, Thin Solid Films 19, 329-337 (1973). "Line Shape Extraction Analysis of Silicon Oxide Layers on Silicon by Channeling Effect Measurements".
33. T. W. Sigmon, W. K. Chu, E. Lugujo, and J. W. Mayer, Appl. Phys. Letters 24 105-107 (1974) "Stoichiometry of Thin Silicon Oxide Layers on Silicon".
34. I. V. Mitchell, M. Kamoshida, and J. W. Mayer, J. Appl. Phys. 42, 4378-4389 (1971) "Channeling-Effect Analysis of Thin Films on Silicon: Aluminum Oxide".
35. W. K. Chu, B. L. Crowder, J. W. Mayer, and J. F. Ziegler, Ion Implantation in Semiconductors and Other Materials ed. by B. L. Crowder, Plenum Press, New York (1973), pp. 225-241 "Ranges and Distribution of Ions Implanted in Dielectrics".
36. J. Gyulai, O. Meyer, J. W. Mayer, and V. Rodriguez, Appl. Phys. Letters 16, 232-234 (1970) "Analysis of Silicon Nitride Layers on Silicon by Backscattering and Channeling Effect Measurements".
37. J. Gyulai, O. Meyer, J. W. Mayer, and V. Rodriguez, J. Appl. Phys. 42, 451-456 (1971) "Evaluation of Silicon Nitride Layers of Various Composition by Backscattering and Channeling-Effect Measurements".
38. O. Meyer and W. Scherber, J. Phys. Chem. Solids 32, 1909-1915 (1971) "Analysis of Silicon Nitride Layers Deposited from  $\text{SiH}_4$  and  $\text{N}_2$  on Si".
39. M. Croset, S. Rigo, and G. Amsel, Appl. Phys. Letters 19, 33-35 (1971) "Investigation of the Composition of Sputtered Silicon Nitride Films by Nuclear Microanalysis".
40. I. V. Mitchell, M. Kamoshida, and J. W. Mayer, Phys. Letters 35A, 21-22 (1971) "Line Shape Extraction from MeV  $\text{He}^+$  Backscattering Energy Spectra: Aluminum Oxide on Silicon".
41. M. Kamoshida, I. V. Mitchell, and J. W. Mayer, Appl. Phys. Letters 18, 292-294 (1971) "Influence of Deposition Temperature on Properties of Hydrolytically Grown Aluminum Oxide Films".
42. M. Kamoshida, I. V. Mitchell, and J. W. Mayer, J. Appl. Phys. 43, 1717-1724 (1972) "Influence of Heat Treatment on Aluminum Oxide Films on Silicon".
43. J. M. Poate, T. M. Buck, and B. Schwartz, J. Phys. Chem. Solids 34, 779-786 (1973) "A Rutherford Scattering Study of the Chemical Composition of Native Oxides on GaP".
44. J. M. Poate, P. J. Silverman, and J. Yahalom, J. Electrochem. Soc. 120, 844-845 (1973) "Anodic Oxide Films on GaP".



45. J. M. Poate, P. J. Silverman and J. Yahalom, *J. Phys. Chem. Solids* 34, 1847-1857 (1973) "The Growth and Composition of Anodic Films on GaP".
46. L. C. Feldman, J. M. Poate, F. Ermanis, and B. Schwartz, *Thin Solid Films* 19, 81-89 (1973) "The Combined Use of He Backscattering and He Induced X-Rays in the Study of Anodically Grown Oxide Films on GaAs".
47. B. C. Dobbs and P. M. Hemenger, Unpublished Data.
48. C. J. Frosch and L. Derick, *J. of the Electrochem. Soc.* 104, 547-552 (1957) "Surface Protection and Selective Masking During Diffusion in Silicon".
49. J. Gyulai, J. W. Mayer, I. V. Mitchell, and V. Rodriguez, *Appl. Phys. Letters* 17, 332-334 (1970) "Outdiffusion Through Silicon Oxide and Silicon Nitride Layers on Gallium Arsenide".
50. J. W. Mayer, Private Communication.
51. R. D. Pashley, California Institute of Technology. Report No. AFCRL-TR-74-0171, January 1974 under Contract F19628-73-C-0174, Work Unit 56380201. "Electrical Properties of Ion Implanted Layers in Silicon and Gallium Arsenide".
52. F. H. Eisen, J. S. Harris, B. Welch, R. D. Pashley, D. Sigurd, and J. W. Mayer, *Ion Implantation in Semiconductors and Other Materials*, ed. by B. L. Crowder, Plenum Press, New York, N.Y. (1972), pp. 631-640 "Properties of Tellurium Implanted Gallium Arsenide".
53. S. T. Picraux, *Ion Implantation in Semiconductors and Other Materials*, ed. by B. L. Crowder, Plenum Press, New York, N.Y. (1972), pp. 641-654 "Vaporization of Ion Implanted GaAs".
54. J. A. Davies, Private Communication.
55. J. S. Williams, Private Communication.

In addition to the above cited publications, two recent books are useful general references:

- A1. G. Dearnaley, J. H. Freeman, R. S. Nelson, and J. Stephen, *Ion Implantation*, American Elsevier Publishing Company, New York (1973).
- A2. *Application of Ion Beams to Metals*, ed. by S. T. Picraux, E. P. Eer Nisse, and F. L. Vook, Plenum Press, New York (1974).